frontiers | Frontiers in Astronomy and Space Sciences

TYPE Original Research
PUBLISHED 14 May 2024
DOI 10.3389/fspas.2024.1335459

OPEN ACCESS

EDITED BY
Esra Bulbul,
Max Planck Institute for Extraterrestrial Physics, Germany

REVIEWED BY
Zhiyuan Ma,
University of Massachusetts Amherst, United States
Swayamtrupta Panda,
Laboratório Nacional de Astrofísica, Brazil

*CORRESPONDENCE
P. G. Boorman,
boorman@caltech.edu

†NASA Postdoctoral Program Fellow

‡NHFP Einstein Fellow

RECEIVED 08 November 2023
ACCEPTED 21 February 2024
PUBLISHED 14 May 2024

CITATION
Boorman PG, Torres-Albà N, Annuar A, Marchesi S, Pfeifle RW, Stern D, Civano F, Baloković M, Buchner J, Ricci C, Alexander DM, Brandt WN, Brightman M, Chen CT, Creech S, Gandhi P, García JA, Harrison F, Hickox R, Kammoun E, LaMassa S, Lanzuisi G, Marcotulli L, Madsen K, Matt G, Matzeu G, Nardini E, Piotrowska JM, Pizzetti A, Puccetti S, Sicilian D, Silver R, Walton DJ, Wilkins DR, Zhao X and The HEX-P Collaboration (2024), The High-Energy X-ray Probe (HEX-P): the circum-nuclear environment of growing supermassive black holes.
Front. Astron. Space Sci. 11:1335459.
doi: 10.3389/fspas.2024.1335459

The High-Energy X-ray Probe (HEX-P): the circum-nuclear environment of growing supermassive black holes

P. G. Boorman[1]*, N. Torres-Albà[2], A. Annuar[3], S. Marchesi[2,4,5], R. W. Pfeifle[6,7†], D. Stern[8], F. Civano[6], M. Baloković[9,10], J. Buchner[11], C. Ricci[12,13], D. M. Alexander[14], W. N. Brandt[15,16,17], M. Brightman[1], C. T. Chen[18,19], S. Creech[20,21], P. Gandhi[22], J. A. García[1,6], F. Harrison[1], R. Hickox[23], E. Kammoun[24,25], S. LaMassa[26], G. Lanzuisi[5], L. Marcotulli[9,10‡], K. Madsen[6], G. Matt[24], G. Matzeu[27], E. Nardini[25], J. M. Piotrowska[1], A. Pizzetti[2], S. Puccetti[28], D. Sicilian[29], R. Silver[6†], D. J. Walton[30], D. R. Wilkins[31], X. Zhao[32] and The HEX-P Collaboration

[1]Cahill Center for Astrophysics, California Institute of Technology, Pasadena, CA, United States, [2]Department of Physics and Astronomy, Clemson University, Kinard Lab of Physics, Clemson, SC, United States, [3]Department of Applied Physics, Faculty of Science and Technology, Universiti Kebangsaan Malaysia, Bangi, Malaysia, [4]Dipartimento di Fisica e Astronomia (DIFA), Università di Bologna, Bologna, Italy, [5]INAF—Osservatorio di Astrofisica e Scienza dello Spazio di Bologna, Bologna, Italy, [6]X-ray Astrophysics Laboratory, NASA Goddard Space Flight Center, Greenbelt, MD, United States, [7]Oak Ridge Associated Universities, NASA NPP Program, Oak Ridge, TN, United States, [8]Jet Propulsion Laboratory, California Institute of Technology, Pasadena, CA, United States, [9]Yale Center for Astronomy and Astrophysics, New Haven, CT, United States, [10]Department of Physics, Yale University, New Haven, CT, United States, [11]Max-Planck-Institut für extraterrestrische Physik, Garching, Germany, [12]Instituto de Estudios Astrofísicos, Facultad de Ingeniería y Ciencias, Universidad Diego Portales, Santiago, Chile, [13]Kavli Institute for Astronomy and Astrophysics, Peking University, Beijing, China, [14]Centre for Extragalactic Astronomy, Department of Physics, Durham University, Durham, United Kingdom, [15]Department of Astronomy and Astrophysics, The Pennsylvania State University, University Park, PA, United States, [16]Institute for Gravitation and the Cosmos, The Pennsylvania State University, University Park, PA, United States, [17]Department of Physics, The Pennsylvania State University, University Park, PA, United States, [18]Science and Technology Institute, Universities Space Research Association, Huntsville, AL, United States, [19]Astrophysics Office, NASA Marshall Space Flight Center, Huntsville, AL, United States, [20]Department of Physics and Astronomy, University of Utah, Salt Lake City, UT, United States, [21]Astrophysics Science Division, SURA/GSFC/CRESST II, Greenbelt, MD, United States, [22]Department of Physics and Astronomy, Faculty of Physical Sciences and Engineering, University of Southampton, Southampton, United Kingdom, [23]Department of Physics and Astronomy, Dartmouth College, Hanover, NH, United States, [24]Dipartimento di Matematica e Fisica, Universitá degli Studi Roma Tre, Roma, Italy, [25]INAF—Osservatorio Astrofisico di Arcetri, Firenze, Italy, [26]Space Telescope Science Institute, Baltimore, MD, United States, [27]European Space Agency (ESA), European Space Astronomy Centre (ESAC), Madrid, Spain, [28]ASI—Agenzia Spaziale Italiana, Via del Politecnico snc, Roma, Italy, [29]Department of Physics, University of Miami, Coral Gables, FL, United States, [30]Centre for Astrophysics Research, University of Hertfordshire, College Lane, Hatfield, United Kingdom, [31]Kavli Institute for Particle Astrophysics and Cosmology, Stanford University, Stanford, CA, United States, [32]Harvard-Smithsonian Center for Astrophysics, Cambridge, MA, United States

Ever since the discovery of the first active galactic nuclei (AGN), substantial observational and theoretical effort has been invested into understanding how massive black holes have evolved across cosmic time. Circum-nuclear obscuration is now established as a crucial component, with almost every AGN observed known to display signatures of some level of obscuration in their X-ray spectra. However, despite more than six decades of effort, substantial

open questions remain: *how does the accretion power impact the structure of the circum-nuclear obscurer? What are the dynamical properties of the obscurer? Can dense circum-nuclear obscuration exist around intrinsically weak AGN? How many intermediate mass black holes occupy the centers of dwarf galaxies?* In this paper, we showcase a number of next-generation prospects attainable with the *High-Energy X-ray Probe* (*HEX-P*[1]) to contribute toward solving these questions in the 2030s. The uniquely broad (0.2–80 keV) and strictly simultaneous X-ray passband of *HEX-P* makes it ideally suited for studying the temporal co-evolution between the central engine and circum-nuclear obscurer. Improved sensitivities and reduced background will enable the development of spectroscopic models complemented by current and future multi-wavelength observations. We show that the angular resolution of *HEX-P* both below and above 10 keV will enable the discovery and confirmation of accreting massive black holes at both low accretion power and low black hole masses even when concealed by thick obscuration. In combination with other next-generation observations of the dusty hearts of nearby galaxies, *HEX-P* will be pivotal in paving the way toward a complete picture of black hole growth and galaxy co-evolution.

KEYWORDS

X-ray, active galactic nuclei, obscuration, black hole, galaxies, Compton-thick, high energy, spectral modeling

1 Introduction

1.1 The prevalence of obscured accretion onto supermassive black holes

It is now well established that obscuration is an omnipresent ingredient in the growth of supermassive black holes. Prime evidence arises from X-ray surveys and population synthesis studies, which have found heavily obscured AGN to dramatically dominate the AGN population at all but the strongest accretion powers, irrespective of redshift (Comastri et al., 1995; Gandhi and Fabian, 2003; Gilli et al., 2007; Treister et al., 2009; Akylas et al., 2012; Buchner et al., 2014; 2015; Ueda et al., 2014; Aird et al., 2015; Brandt and Alexander, 2015; Lansbury et al., 2017; Ananna et al., 2019; Ananna et al., 2022; Ricci et al., 2022). Though some portion resides on galactic scales (Buchner et al., 2017; Gilli et al., 2022; Andonie et al., 2023), the densest *Compton-thick* obscuration ($N_{\rm H} > 1.5 \times 10^{24}$ cm^{-2})[2] is expected to reside on circum-nuclear parsec scales, similar to the sizes invoked in unified schemes (Antonucci, 1993; Urry and Padovani, 1995; Netzer, 2015; Ramos Almeida and Ricci, 2017).

The Compton-thick fraction is often inferred to be similarly substantial to the obscured (i.e., 10^{22} cm^{-2} < $N_{\rm H}$ < 1.5×10^{24} cm^{-2}) AGN population across cosmic time (see discussion in Comastri et al., 2015; Civano et al., 2023), even after considering the non-trivial dependence with the nature of the intrinsic X-ray-emitting corona and/or accretion flow (Gandhi et al., 2007; Vasudevan et al., 2016; Kammoun et al., 2023; Piotrowska et al., 2023). For example, the latest population synthesis models from Ananna et al. (2019) constrain the abundance of Compton-thick AGN to be 50% ± 9% within z = 0.1 and 56 ± 9% within z = 1 of all AGN.

Theoretical models of supermassive black hole growth additionally suggest that enhanced circum-nuclear obscuration is intricately linked to not only just supermassive black hole accretion (Fabian, 1999) but also galaxy–supermassive black hole co-evolution (Anglés-Alcázar et al., 2021) and galaxy–galaxy interactions as a whole (Springel et al., 2005; Hopkins et al., 2006; Pfeifle et al., 2023). Although it is still uncertain as to the exact role that the dense circum-nuclear obscurer plays, some viable options include a feeding reservoir for the central black hole (Storchi-Bergmann and Schnorr-Müller, 2019) or by-product of the central engine itself (Wada, 2012). Compton-thick AGN are hence pertinent targets to unveil the drivers of galaxy growth and understand the co-evolution between supermassive black holes and galaxies, as highlighted in the Astro2020 Decadal Survey[3].

However, Compton-thick AGN are one of the most difficult classes of AGN to detect and study (Hickox and Alexander, 2018; Asmus et al., 2020; Brandt and Yang, 2022). For energies E < 10 keV, the intrinsic X-ray flux from the corona is mostly extinguished via the photoelectric effect and only a few percent of the intrinsic flux escapes (Gupta et al., 2021). Some fluxes survive in the form of narrow X-ray fluorescent lines at specific energies, with those arising from neutral iron K at 6.4 keV (rest

1 https://hexp.org

2 The Compton-thick threshold is generally adopted to be the inverse of the Thomson-scattering cross section, though the actual threshold will depend on other factors, such as abundances. See Section 2.1 and Equation 2.3 of the `MYtorus` manual (http://mytorus.com/mytorus-instructions.html) for more information.

3 https://www.nationalacademies.org/our-work/decadal-survey-on-astronomy-and-astrophysics-2020-astro2020

frame) typically being the strongest. The remaining AGN fluxes observed are dominated by X-ray photons that have undergone Compton recoil in one or multiple scatterings and escaped the obscurer, giving rise to the underlying Compton-scattered continuum. At ~20–40 keV, the continuum peaks into a broad Compton hump with overall shape determined by the geometry of the obscurer (Matt et al., 2000; Murphy and Yaqoob, 2009; Buchner et al., 2019).

1.2 X-ray spectroscopic modeling of circum-nuclear obscuration

Many X-ray spectroscopic models describing the broadband X-ray emission from obscured AGN are available to date with varying geometric prescriptions for the obscurer. Such variations can be broadly separated into (1) *ad hoc* (i.e., computationally convenient) geometries, such as smooth density obscurers (`etorus`, Ikeda et al., 2009; `MYtorus`, Murphy and Yaqoob, 2009; `BNsphere`, Brightman and Nandra, 2011a; `RXtorus`, Paltani and Ricci, 2017; `borus`, Baloković et al., 2018; 2019; `wedge`, Buchner et al., 2019), clumpy obscurers (`Ctorus`, Liu and Li, 2014; `XCLUMPY`, Tanimoto et al., 2019; `UXCLUMPY`, Buchner et al., 2019), and combinations of different unique geometric components (see the polar gas simulations from Liu et al., 2019; McKaig et al., 2022 or the broadband physical model of the Circinus Galaxy in Andonie et al., 2022) and (2) geometries that emerge from radiative hydrodynamical simulations (`warpeddisk`, `radiativefountain`; Buchner et al., 2021). There has also been a surge in the availability of ray tracing packages designed to enable the production of bespoke user-defined X-ray spectral models in arbitrary geometries and the inclusion of additional physical processes (MONACO: Odaka et al., 2011 and Odaka et al., 2016; RefleX[4]: Paltani and Ricci, 2017 and Ricci and Paltani, 2023; XARS[5]: Buchner et al., 2019; SKIRT[6]: Vander Meulen et al., 2023).

The ability for accurate and precise inference from circum-nuclear obscuration models with ever-increasing numbers of fit parameters is currently met by substantial challenges. The first is exploring the degenerate and multi-modal (i.e., non-identifiable) parameter spaces inherent to the spectral model libraries that result from ray tracing simulations. A typical model to explain the 0.2–80 keV spectra of obscured AGN can consist of $\gtrsim 10$ parameters describing the intrinsic X-ray spectrum, the geometric prescription of the surrounding circum-nuclear obscurer, and other contaminating soft X-ray emissions. The corresponding multi-dimensional parameter spaces are very complex and do not necessarily lead to unique spectral solutions when compared with alternative geometric models of the obscurer (Saha et al., 2022; Kallová et al., 2023). As such, parameter exploration, model verification, and model comparison are all non-trivial and can be exceedingly expensive to compute with increased numbers of fit parameters (van Dyk et al., 2001; Buchner et al., 2014; Buchner and Boorman, 2023). Increased complexity of obscuration models will also require more ray tracing simulations to compute. Due to the corresponding trade-off between exploring fewer geometries *versus* coarser parameter grid resolution, the conventional use of multi-dimensional tables and grid interpolation to fit spectra may become obsolete entirely. A promising alternative is emulation, which has been shown to accelerate the computation time associated with radiative transfer simulations (Kerzendorf et al., 2021; Rino-Silvestre et al., 2022) and avoid the requirement for coarse gridding of parameters into multi-dimensional tables entirely (Matzeu et al., 2022).

The second challenge is the observational requirement for high-quality *broadband* spectroscopy of Compton-thick AGN to test complex physical models. Valuable insights have been attained with focusing X-ray optics < 10 keV, typically capable of isolating the Fe Kα complex and underlying reflection continuum from contaminating non-AGN spectral features (Risaliti et al., 1999; Brightman and Nandra, 2011a; LaMassa et al., 2017). However, without similar sensitivities > 10 keV, strong ambiguity still remains relating to the shape of the Compton hump (see discussion in Brightman et al., 2015; LaMassa et al., 2019; 2023). Hard X-ray sensitivities provided by coded aperture masks have limited previous studies to higher observed X-ray fluxes (Yaqoob, 2012; Gandhi et al., 2013; 2015; Ricci et al., 2017c) and reduced spectral resolution that is insufficient to strongly constrain geometrical properties of the circum-nuclear environment (see discussion in Baloković, 2017; Tanimoto et al., 2022).

NuSTAR (Harrison et al., 2013) provided the first focusing hard X-ray telescope in orbit, opening a new era into the pursuit and understanding of heavily obscured accretion onto supermassive black holes (see Section 2). To date, *NuSTAR* has provided the most sensitive insights into the X-ray obscuration of the brightest Compton-thick AGN known (Arévalo et al., 2014; Puccetti et al., 2014; Bauer et al., 2015; Puccetti et al., 2016), as well as the wider population identified previously with wide-field hard X-ray monitoring surveys (Annuar et al., 2015; Gandhi et al., 2017; Marchesi et al., 2017; 2019b; Torres-Albà et al., 2021; Traina et al., 2021; Zhao et al., 2021; Pizzetti et al., 2022; Silver et al., 2022; Tanimoto et al., 2022). *NuSTAR* has also enabled unambiguous Compton-thick line-of-sight column density classifications for a bulk of the previously published candidate Compton-thick sources that had not been detected > 10 keV before (Baloković et al., 2014; Gandhi et al., 2014; Ptak et al., 2015; Boorman et al., 2016; Masini et al., 2016; Annuar et al., 2017; Ricci et al., 2017; LaMassa et al., 2019; Kammoun et al., 2020). Broadband X-ray spectroscopy has thus proven to be a crucial tool for understanding the obscurer, provided consistent sensitivities are attainable with simultaneous soft X-ray observations across the entire passband (Marchesi et al., 2018; Marchesi et al., 2019a).

Additional complexities arising from the symbiotic relationship between the central engine and the obscurer can introduce systematics, for example, the relationship between the black hole mass-scaled luminosity and covering factor (Fabian et al., 2008; Ricci et al., 2017d).

4 https://www.astro.unige.ch/reflex/

5 https://github.com/JohannesBuchner/xars

6 https://skirt.ugent.be/root/_contributing.html#ContributingRepositories

1.3 Complex structure revealed by variability

There is mounting evidence that the obscurer can be clumpy rather than smooth. This was initially motivated by infrared spectra of AGN, which showed less prominent silicate features than expected from smooth obscuration models (Jaffe et al., 2004; Elitzur, 2006; Hönig and Beckert, 2007; Risaliti et al., 2007; Nenkova et al., 2008). Models such as chaotic cold accretion (Gaspari et al., 2013; Gaspari et al., 2015; Gaspari et al., 2020) suggest clumpy accretion from random angles onto the central 100 pc induced by radiative cooling and turbulence (see Rose et al., 2019; Gaspari et al., 2020; Maccagni et al., 2021; Temi et al., 2022). Obscurer geometries arising from radiation-driven outflows also can produce dynamic, filamentary, and clumpy structures (Vollmer and Duschl, 2002; Wada, 2012; Chan and Krolik, 2016, and references therein). Such clumpy/filamentary models of AGN obscuration predict observed changes in the line-of-sight obscuration.

In X-rays, an inhomogeneity in the circum-nuclear material can vary (i) the accretion luminosity and/or (ii) obscuration level. Such changes can be detected and disambiguated with sufficiently sensitive time-resolved X-ray spectroscopy with a wide-enough passband (Ricci and Trakhtenbrot, 2022). For line-of-sight column density variations $\Delta\ N_{\rm H} \lesssim 10^{23}$ cm^{-2}, the photoelectric turnover is at $\lesssim$ 10 keV and has been used to robustly confirm obscuration variations (Risaliti et al., 2002; 2005; Markowitz et al., 2014). However, for variations $\Delta\ N_{\rm H} \gtrsim 10^{23}$–$10^{24}$ cm^{-2}, sensitive broadband spectroscopy is advantageous to provide constraints on the underlying absorbed spectrum below 10 keV and the reprocessed spectrum above 10 keV to avoid strong degeneracy between the spectral slope, obscuration level, and amount of reprocessing (Walton et al., 2014; Rivers et al., 2015; Lefkir et al., 2023). Decoupling such large changes in obscuration from intrinsic flux variations exclusively in Compton-thick AGN is currently even less represented in the literature, owing in part to the observational demand for observing variations in the Compton hump that are non-trivial to disentangle at $\gtrsim$ 10–20 keV in all but the brightest targets (Puccetti et al., 2014; Marinucci et al., 2016; Nardini, 2017; Zaino et al., 2020; Kayal et al., 2023).

Column density variations are expected to occur over periods of time from ~1 day up to several months, assuming a typical range of obscuring cloud filling factors, velocities, and distances from the accreting black hole (Nenkova et al., 2008). Tentative column density variability timescales on the order of years also exist (Gandhi et al., 2017; Masini et al., 2017; Laha et al., 2020; Torres-Albà et al., 2023), but additional sensitive monitoring is required to quantify its prevalence in the obscured AGN population. Thus, X-ray obscuration variability is a powerful tool for providing reliable constraints on the location of obscuring clouds and their distances from the accreting supermassive black hole (Markowitz et al., 2014; Buchner et al., 2019). By combining numerous epochs of broadband X-ray observations with physical obscuration models, the global properties of the circum-nuclear environment (such as covering factor and average column density) can be decoupled from the epoch-dependent variable components to provide the tightest constraints on obscurer properties in the heavily obscured AGN population currently known (Ricci et al., 2016; Baloković et al., 2018; Marchesi et al., 2022; Pizzetti et al., 2022; Kayal et al., 2023; Torres-Albà et al., 2023). For such observations, simultaneous observations from ~ 0.2–80 keV are essential. These are challenging to achieve, currently requiring the coordination of complementary missions (e.g., *XMM-Newton* and *NuSTAR*), which has limited the sample size for such studies (see Section 4).

1.4 The circum-nuclear environment at low accretion power

Volume-limited multi-wavelength surveys have revealed that the majority of supermassive black holes in the nearby universe are underfed (Ho, 1997, 2008; Baldi et al., 2018, 2021a, 2021b; Williams et al., 2022). This implies that the majority of local galaxies host low-luminosity AGN, often parameterized to have bolometric luminosities $L_{\rm bol} \lesssim 10^{42}$ erg s^{-1}, and/or Eddington-scaled bolometric luminosities (also known as the Eddington ratio) of $\lambda_{\rm Edd} = L_{\rm bol}/L_{\rm Edd} \lesssim 10^{-3}$ (Elitzur, 2006; Hönig and Beckert, 2007; Kawamuro et al., 2016). However, our understanding of the circum-nuclear environment in AGN at low luminosities and accretion powers is currently very incomplete.

Low-luminosity AGN are known to lack an ultraviolet bump in their spectral energy distribution (Ho, 1999; Nemmen et al., 2006; Eracleous et al., 2010) and share similar characteristics to low-luminosity/quiescent accreting stellar mass black holes (Nagar et al., 2005; Körding et al., 2006; Svoboda et al., 2017; Fernández-Ontiveros and Muñoz-Darias, 2021; Moravec et al., 2022), suggesting the absence of a standard optically thick, geometrically thin accretion disc (Shakura and Sunyaev, 1973). At X-ray wavelengths, the absence of Fe Kα emission lines and/or the Compton hump in some low-luminosity AGN also supports this notion, indicating the truncation or absence of a standard accretion disc (Terashima, 2002; González-Martín et al., 2009; Younes et al., 2011; Ursini et al., 2015; Young et al., 2018; Younes et al., 2019; Osorio-Clavijo et al., 2022). Some studies have predicted the collapse and disappearance of the broad-line region and obscuring structure in low-luminosity AGN due to insufficient radiation pressure (Elitzur, 2006; Hönig and Beckert, 2007; Elitzur and Ho, 2009). Although there is some observational evidence supporting these predictions, data are often limited due to the relative difficulty of selecting and studying low-luminosity AGN relative to their more luminous counterparts (Maoz et al., 2005; Ho, 2008; Trump et al., 2011; Hernández-García et al., 2016; Ricci et al., 2017d; González-Martín et al., 2017). Measurements of the obscuring covering factor on a source-by-source basis in large samples via X-ray spectroscopic modeling have provided additional clues supporting this notion, though with considerable uncertainties (Brightman and Nandra, 2011b; Vasudevan et al., 2013; Brightman et al., 2015; Baloković, 2017).

1.5 Accreting intermediate mass black holes

Large numbers of intermediate mass black holes with masses $M_{\rm BH} \sim 10^2$–10^5 M$_\odot$ are required to exist throughout cosmic history to give rise to the $\sim 10^9$ M$_\odot$ supermassive black holes observed within mere hundreds of million years from the Big Bang

(Bañados et al., 2018) up to the present day. A large ongoing challenge, however, is to observationally identify intermediate mass black holes and to understand how they were formed (Greene et al., 2020). Dwarf galaxies are useful to search for intermediate mass black holes. To explain their low masses, dwarf galaxies are expected to have undergone fewer mergers than more massive galaxies that in turn restricts the availability of fuel for the central black holes to grow. Dwarf galaxies in the local universe are hence expected to contain the seeds of the first supermassive black holes, and the dwarf galaxy black hole occupation fraction is a crucial piece of the puzzle (Volonteri et al., 2008; Volonteri, 2010; Greene, 2012; Reines, 2022).

A useful strategy is to search for intermediate mass black hole signatures during episodes of accretion as AGN. The difficulty is that any biases imposed on selecting accreting supermassive black holes in AGN are exacerbated in the case of intermediate mass black holes in low-mass galaxies. Dwarf galaxies often have high levels of star formation that can be significantly stronger than the optical emission associated with the accretion disc surrounding accreting intermediate mass black holes (Moran et al., 2014; Trump et al., 2015). Optical spectroscopy has proven to be a useful tool for identifying unobscured dwarf AGN signatures (Greene and Ho, 2004; 2007; Reines et al., 2013; Baldassare et al., 2018). However, this technique requires that host galaxy dilution be minimal and that the AGN be largely unobscured while accreting at high rates, close to the Eddington limit. X-ray observations are less affected by host galaxy contamination but soft X-rays can be readily absorbed leading to the same biases encountered for more massive black holes in AGN (Brandt and Alexander, 2015; Hickox and Alexander, 2018). Broadband X-ray observations that include hard X-rays are hence crucial to disentangle obscured accreting massive black holes from individual host galaxy X-ray binaries that often have different predicted hard X-ray spectral shapes (see discussion in Lehmer et al., 2023). Detailed broadband X-ray spectroscopic studies of obscured massive black holes in low-mass galaxies are currently rare though due to the requirement for sufficient sensitivities (Ansh et al., 2023; Mohanadas and Annuar, 2023).

1.6 The *HEX-P* perspective

The *High-Energy X-ray Probe* (*HEX-P*; Madsen et al., 2023) is a probe-class mission concept that offers sensitive coverage (0.2–80 keV) of the X-ray spectrum with exceptional spectral, timing, and angular capabilities. It features a high-energy telescope (HET) that focuses hard X-rays, and one low-energy telescope (LET) that focuses soft X-rays in a parallel structure.

The LET (0.2–25 keV) consists of a segmented mirror assembly coated with Iridium on monocrystalline silicon that achieves a half power diameter of 3.5" and a low-energy DEPFET detector of the same type as the Wide Field Imager (WFI; Meidinger et al., 2020) that will be onboard *Athena* (Nandra et al., 2013). It has 512 × 512 pixels that cover a field of view of 11.3' × 11.3'. It has an effective passband of 0.2–25 keV and a full frame readout time of 2 ms, which can be operated in a 128- and 64-channel window mode for higher count-rates to mitigate pile-up and achieve faster readout. Pile-up effects remain below an acceptable limit of ~1% for fluxes up to ~100 mCrab in the smallest window configuration. Excising the core of the PSF, a common practice in X-ray astronomy, will allow for observations of brighter sources, with a typical loss of up to ~ 60% of the total photon counts.

The HET (2–80 keV) consists of two co-aligned telescopes and detector modules. The optics are made of Ni-electroformed full-shell mirror substrates, leveraging the heritage of *XMM-Newton* (Jansen et al., 2001), and coated with Pt/C and W/Si multilayers for an effective passband of 2–80 keV. The high-energy detectors are of the same type as those onboard *NuSTAR* (Harrison et al., 2013), and they consist of 16 CZT sensors per focal plane, tiled 4 × 4, for a total of 128 × 128 pixels spanning a field of view slightly larger than that for the LET, of 13.4' × 13.4'.

The unique improvements yielded by *HEX-P* will provide significant advancements in the study of supermassive black hole growth. Enhanced sensitivity above 10 keV relative to *NuSTAR* will enable detailed modeling constraints of the faintest Compton-thick AGN currently known (see Section 5; Pfeifle et al., 2023) and the completion of the local AGN census that is predominantly restricted by our ability to uncover Compton-thick AGN (Asmus et al., 2020; Civano et al., 2023). The strictly simultaneous broadband coverage will also remove any ambiguity associated with spectral component variability that can significantly affect the inference of key system parameters (see discussion in Baloković et al., 2018; Baloković et al., 2021; Torres-Albà et al., 2023; Section 4). Lastly, the extended passband of the LET up to energies of ~ 25 keV will provide sensitive overlapping X-ray spectroscopy in both *HEX-P* telescopes. The energy range ~ 5–8 keV contains the iron K lines which hold enormous diagnostic value for the structure of the circum-nuclear obscurer when combined with the underlying continuum ≳ 10 keV (Baloković et al., 2018). Having three individual instruments across this wavelength range will also provide independent verification for blue-shifted absorption features arising from outflowing material that have proven difficult to detect in heavily obscured AGN to date (Matzeu et al., 2019). At higher energies, the passband between ~8 and 25 keV encompasses the first inflection point of the Compton hump that holds exciting potential as a fingerprint-like identifier for the circum-nuclear obscurer(s) surrounding the AGN (see Buchner et al., 2019; Buchner et al., 2021).

The paper is organized as follows: Section 2 presents the latest compilation of published Compton-thick AGN within ~ 400 Mpc, confirmed in part by *NuSTAR* observations. To our knowledge, this is the largest compilation of local Compton-thick AGN constructed to date and combines sources selected at a variety of different wavelengths. In Section 3, we present a detailed X-ray spectral analysis of local megamaser AGN, highlighting the prospects for *HEX-P* and next-generation obscuration models to study the effects of radiative feedback from AGN. Section 4 showcases the future possibilities with multi-epoch studies attainable with high sensitivity, strictly simultaneous, broadband X-ray spectroscopy. The current and future prospects behind the behavior of dense AGN obscurers at extremely low luminosities are discussed in Section 5, followed by the prospects for detecting faint obscured AGN in dwarf galaxies in Section 6. We then provide a quantitative estimate of the volume accessible by *HEX-P* for robust characterization of Compton-thick obscuration and compare it to the current state of the art in Section 7. We present our summary in Section 8.

All the *HEX-P* simulations presented in this work were produced with a set of response files that represent the observatory performance based on current best estimates as of Spring 2023

(v07; see Madsen et al., 2023 for corresponding LET and HET sensitivity curves). The effective area is derived from ray tracing of the mirror design that includes obscuration by all known structures. The detector responses are based on simulations performed by the respective hardware groups, with an optical blocking filter for the LET and a Beryllium window and thermal insulation for the HET. The LET background was derived from a Geant4 simulation (Eraerds et al., 2021) of the WFI instrument, and the HET background was derived from a Geant4 simulation of the *NuSTAR* instrument. Both background simulations adopt the planned L1 orbit for *HEX-P*.

2 The Database of Compton-thick AGN

To understand the Compton-thick AGN population uncovered to date and as a natural starting point for our *HEX-P* simulations, we construct a comprehensive list of Compton-thick AGN identified in the literature. To ensure accurate modeling of the underlying Compton scattered continuum in such sources, we limit our search to targets confirmed with spectral modeling that included *NuSTAR* data. Whilst other X-ray instruments such as the *Suzaku*/Hard X-ray Detector, the *Swift*/Burst Alert Telescope, and *INTEGRAL* have provided hard X-ray spectroscopic constraints for some Compton-thick AGN (Yaqoob, 2012; Gandhi et al., 2013; Gandhi et al., 2015; Vasylenko et al., 2013; Ricci et al., 2015), we limit ourselves to the requirement for *NuSTAR* due to its 100-fold increase in sensitivity above 10 keV relative to previous missions (Harrison et al., 2013). The resulting Database of Compton-thick AGN (DoCTA) was created as follows:

1. *Literature search*: We first identified a list of peer-reviewed publications with a NASA ADS[7] search query for any refereed paper containing the phrase 'Compton-thick' and '*NuSTAR*' somewhere in the main body of text. The search returned 690 refereed publications.
2. *Literature refinement*: We manually filtered through the list of publications identified in Step 1, finding ~90 publications that use AGN X-ray spectroscopic modeling with *NuSTAR* (often but not always complemented by soft X-ray spectroscopy from a different instrument) to constrain line-of-sight column density via obscuration models of some form.
3. *Line-of-sight column density*[8]: We sought to extract the line-of-sight column density of each system for every acceptable model fit presented per publication. Our reasoning behind this strategy was to be as complete with the literature as possible, enabling inclusion of sources that are classified as Compton-thick with a specific model setup, but not in others. A number of sources have line-of-sight column density measurement upper bounds *consistent* with the Compton-thick limit, but to be conservative, we only consider sources with at least one line-of-sight column density measurement that is lower 90% confidence bound above a Compton-thick threshold of 1.5×10^{24} cm^{-2}, corresponding to the inverse Thomson cross-section.
4. *Computing unabsorbed luminosities:* To understand the fundamental demographics of the sample, we next estimated intrinsic luminosity. Given the inevitably large number of local AGN selected, a large number of redshift-independent distances are available for the sources. We cross-matched the initial set of objects from Step 3 with the NASA Extragalactic Database[9] using sexagesimal coordinates to remove duplicates arising from different published identifiers. We then downloaded all redshift-independent distances per source and used the median distance for sources where one or more values were available. To overcome possible effects from discrepant distance estimates to a given source, we additionally store the distances used by each work and manually correct intrinsic 2–10 keV luminosities into fluxes when intrinsic fluxes are not provided. We use the median redshift-independent distance listed on NED where available, otherwise the luminosity distance is calculated assuming the cosmological parameters H_0 = 70.0 km s^{-1} Mpc^{-1}, Ω_Λ = 0.7, and Ω_M = 0.3.

Section 8 presents all published values of line-of-sight column density and intrinsic flux for each of the 66 Compton-thick AGN in DoCTA. A wide range of possible scientific applications are clearly provided with DoCTA. The primary focus for this work is to assess the ability of current circum-nuclear obscuration models paired with modern broadband X-ray spectral sensitivity to provide unique solutions for intrinsic luminosity and line-of-sight column density, in the absence of considerable source variability (see Figure 3 and Section 4 for more information on this assumption).

Figure 1 presents the distance vs. unabsorbed 2–10 keV X-ray luminosity for every intrinsic 2–10 keV luminosity measurement of every source in DoCTA. The *left* panel shows that DoCTA is limited to $\lesssim$100 Mpc for the conventional Seyfert definition with unabsorbed 2–10 keV luminosity, $L_{2-10\ \mathrm{keV}} > 10^{42}$ erg s^{-1}. Beyond ~250 Mpc, only quasars ($L_{2-10\ \mathrm{keV}} > 10^{44}$ erg s^{-1}) have been found as Compton-thick. Overall, there is a significant range of published intrinsic luminosities per source, with some estimates ranging over >3 orders of magnitude in the most extreme cases. This trend is shown in Figure 1, which marks the range in intrinsic luminosity reported in the spectral fits included in DoCTA. Under the assumption of negligible source variability (see Figure 3), such variations can arise from choosing different circum-nuclear obscuration models. This also leads to a significant systematic uncertainty in parameter inference (i.e., not only unabsorbed luminosity but also line-of-sight column density and covering factors). It is concerning that this occurs even in the local universe where the observing conditions are optimal (e.g., bright fluxes thanks to source proximity and spatial separation of nearby nuclear contaminants). Some sources, particularly at larger distances, appear to show little luminosity variation. However, this may be because

7 https://ui.adsabs.harvard.edu

8 We refer to "line-of-sight" or "angle-averaged" column densities throughout this work to distinguish between the Thomson depth of material along the line-of-sight and the angle-averaged Thomson depth of material out of the line-of-sight, respectively.

9 https://ned.ipac.caltech.edu

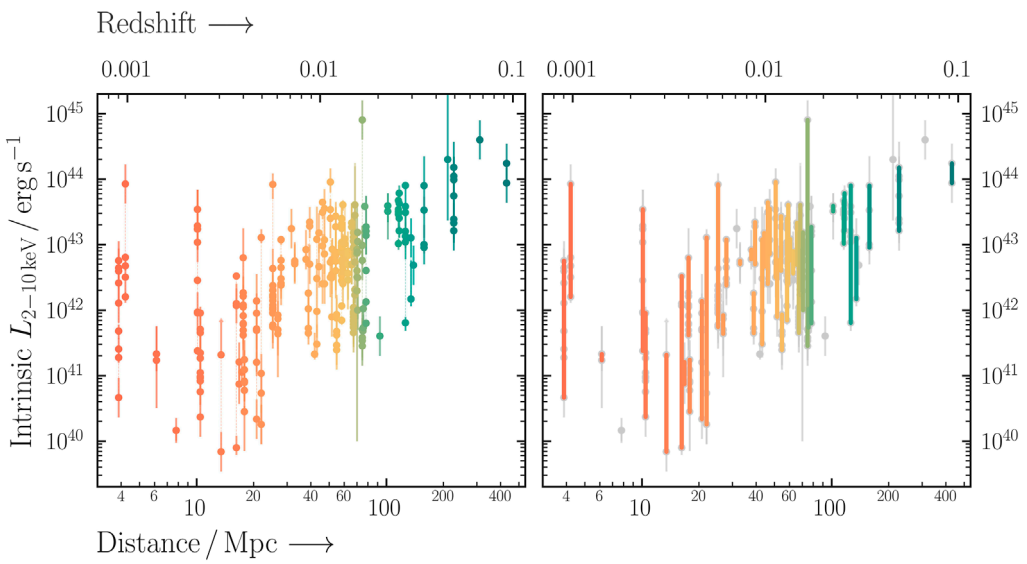

FIGURE 1
(*Left*) Distance vs. intrinsic (i.e., unabsorbed) 2–10 keV luminosity reported in the literature for all local Compton-thick AGN. We have only included Compton-thick classifications that included *NuSTAR* data in the spectral analysis. Multiple reported luminosities for a single source are connected by a vertical dashed line. (*Right*) Same as the *left* panel, with vertical bars indicate the range in best-fit luminosities for each source. For most sources, the reported luminosities vary over one to two orders of magnitude and, in some extreme cases, over three orders of magnitude. The color coding is used to distinguish between different sources and does not correspond to a physical parameter. For analyses lacking an intrinsic flux uncertainty measurement, we conservatively assume a symmetric uncertainty in logarithmic space of 0.3 dex.

those targets have been studied in fewer publications than famous nearby sources (e.g., the Circinus Galaxy and NGC 4945).

Figure 2 presents distance vs. line-of-sight column density from the literature for every available measurement of every source in DoCTA. Similar to Figure 1, we find a significant range of measured line-of-sight column densities. Such a range can arise from subtle differences in the physical properties of the obscurer assumed in different models. For example, line-of-sight column density is inextricably linked to predicted intrinsic luminosity since an increase in line-of-sight column density requires an increase in intrinsic luminosity to explain the additional absorption. Alternatively, parameter differences across obscuration models can arise from how the parameters are represented in the corresponding table models used in the spectral fitting (e.g., the number of parameter grid points). A primary effect of such confusion is that a significant number of sources have published measured line-of-sight column densities both above and below the Compton-thick limit (horizontal dashed line) to 90% confidence. Such uncertainty can clearly have fundamental model-dependent effects on measurements of the Compton-thick AGN abundance for example. A subset of the DoCTA sources are known as changing-obscuration AGN (Ricci and Trakhtenbrot, 2022), in which the line-of-sight column density varies both below and above the Compton-thick threshold (e.g., NGC 1358; Marchesi et al., 2022). However, Compton-thick changing-obscuration events are rarely observed at present, meaning that the wide range in line-of-sight column densities is not expected to be dominated by changing-obscuration AGN.

A large number of different model prescriptions for the obscuration-based reprocessed spectrum in AGN are available in the literature today, as well as different bespoke setups that incorporate those models. A prime example of the latter is the use of decoupled models, in which the global average properties of the reprocessor are decoupled from the reprocessing effects along the line-of-sight (see Yaqoob, 2012 for a detailed review of such techniques). On the practical side, decoupled model fitting often improves the fit due to the larger range of spectral shapes attainable. On the theoretical side, it can be interpreted as flux variability or line-of-sight column density variations arising from a clumpy obscurer. As such, decoupled model setups can often include an overall scaling of the intrinsic continuum relative to the reprocessed one. LaMassa et al. (2019) have shown the effect of manually altering the contribution from reprocessing in the broadband spectral fitting of NGC 4968, finding that an increase in reprocessed flux corresponds to an overall decrease in intrinsic continuum flux, as expected.

Many obscured AGN are variable in hard X-rays (Torres-Albà et al., 2023), such as bright Compton-thick AGN (Puccetti et al., 2014; Marinucci et al., 2016; Marchesi et al., 2022). To understand the high-energy (E > 10 keV) spectral constraints for the DoCTA population and to qualitatively understand the possibility of variability impacting the ranges shown in Figures 1, 2, we extracted all archival *NuSTAR* data available per source with > 10 ks of net exposure time in both focal plane modules (FPMA and FPMB). While intra-observation variability is not unheard of in Compton-thick AGN (Puccetti et al., 2014), it is currently rare in the literature, so we choose to extract epoch-averaged spectra. The *NuSTAR* data for both FPMA and FPMB were processed using the *NuSTAR* Data Analysis Software package within `HEAsoft`. The task `nupipeline` was used to generate cleaned event files. Spectra and corresponding response files were generated using `nuproducts` with circular source regions of 20 pixels (~49") and background regions as large as possible on the same detector as the target. Each

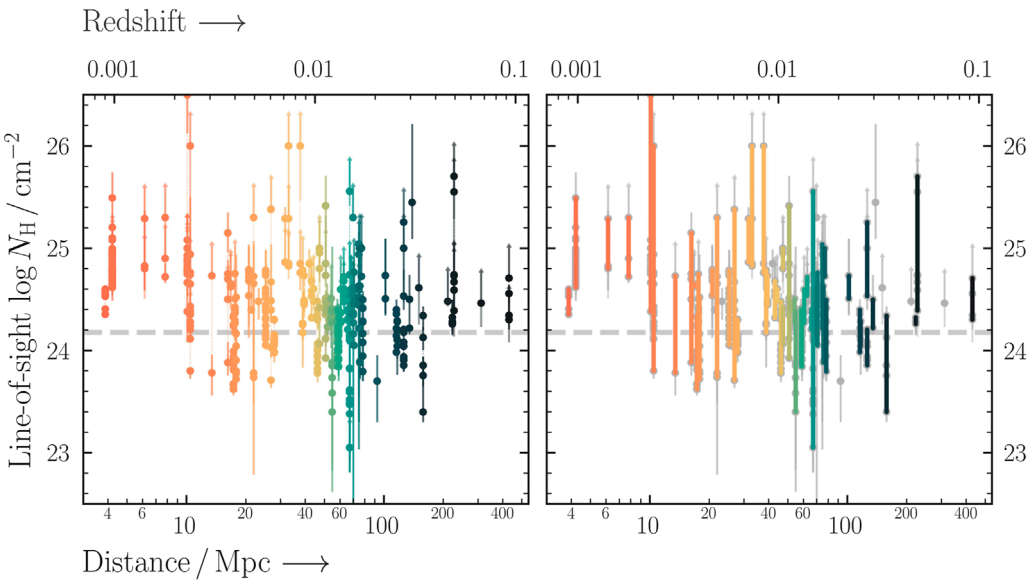

FIGURE 2
Left and *right* panels are the same as in Figure 1, apart from the reported line-of-sight column density that is shown on the vertical axis. The Compton-thick threshold adopted for this work is shown with a horizontal dashed line. The large range between reported line-of-sight log N_H values and the large number of lower limits per source in the Compton-thick regime highlights the challenge with current models to constrain the upper boundary of column density for Compton-thick AGN. We additionally note that the upper bound for each N_H measurement considered during fitting depends on a given specific model setup. The large range itself is fundamentally due to modeling degeneracies remaining in low signal-to-noise ratio of hard X-ray data and variability in time relative to the complementary soft X-ray observations. Both issues will be directly addressed with *HEX-P*.

spectrum was then binned using the optimal binning scheme of Kaastra and Bleeker (2016).

Figure 3 presents residuals in the form of `(data-model)/error` for every extracted *NuSTAR* spectrum after fitting a simple `zcutoffpl` model in PyXspec to the first observed spectrum per source in the 3–78 keV band. We then plot the residuals for every observation per source relative to the fit of the original spectral fit to highlight source variability that has been detected by *NuSTAR*. The figure is organized vertically into bins of *NuSTAR*/FPMA 3–78 keV signal-to-noise ratio, increasing from the bottom to top row. A number of interesting features are visible from Figure 3. First, there is a large diversity in shapes of the Fe K complex (rest frame 6.4 keV is marked with a vertical line in each panel) and Compton hump across the sample. A number of factors can contribute to observed spectral diversity in heavily obscured AGN, whether it be from contamination in the Fe K band and softer energies ($E \lesssim 8$ keV) arising from competing spectral components (Annuar et al., 2015; Reynolds et al., 2015; Farrah et al., 2016; Gandhi et al., 2017) or due to the structure of the obscurer itself at $E \gtrsim 8$ keV (Buchner et al., 2019; 2021). As noted by Bauer et al. (2015), it is physically unlikely for a single-column density obscurer to surround AGN and a plausible alternative could be a continuous distribution of obscurers with varying column densities and other geometric parameters, consistent with galactic molecular cloud studies (Goodman et al., 2009).

Most of the highest signal-to-noise ratio Compton-thick AGN on the top row of Figure 3 display significant spectral variability with *NuSTAR* (Puccetti et al., 2014; Marinucci et al., 2016; Marchesi et al., 2022; Kayal et al., 2023). Only a small number of targets have been selected for *NuSTAR* follow-up because of known variability, and with sufficient sensitivity, repeated observations of others may well show that obscurer-based variability is ubiquitous amongst Compton-thick AGN. For the remainder of the DoCTA population, there are either insufficient *NuSTAR* epochs to search for variability (see panels with $N_{obs} = 1$ in the figure) or the visual difference in the observed reflection spectra is small. Furthermore, the lowest third of DoCTA sources in terms of signal-to-noise ratio have insufficient data quality to reveal any spectral variability in detail (see Section 4 for further discussion).

HEX-P is optimized in many ways to guide the future development of X-ray spectral models. First, the improved broadband sensitivity achieved by reducing the background level will result in a significant improvement in the observed signal-to-noise ratio for the bulk of the Compton-thick AGN population present in DoCTA. Such improvements will fundamentally decrease the number of possibilities for non-unique spectral fits in which parameter posteriors are significantly different. Second, the extended range of the LET to energies > 10 keV means that there will be three instruments in total providing sensitive spectra over the energy range corresponding to the inflection point of the Compton hump. Detailed spectral modeling of Compton hump diversity is currently an under-used resource for constraining the covering factor of material with different column densities surrounding the central engine (Buchner et al., 2019). Lastly, the simultaneous broadband focusing capabilities of *HEX-P* are a novel concept amongst previous, current, and future planned X-ray missions. Broadband coverage removes any possible issues that can arise from variability or significantly mismatched data quality in soft and hard X-ray bands.

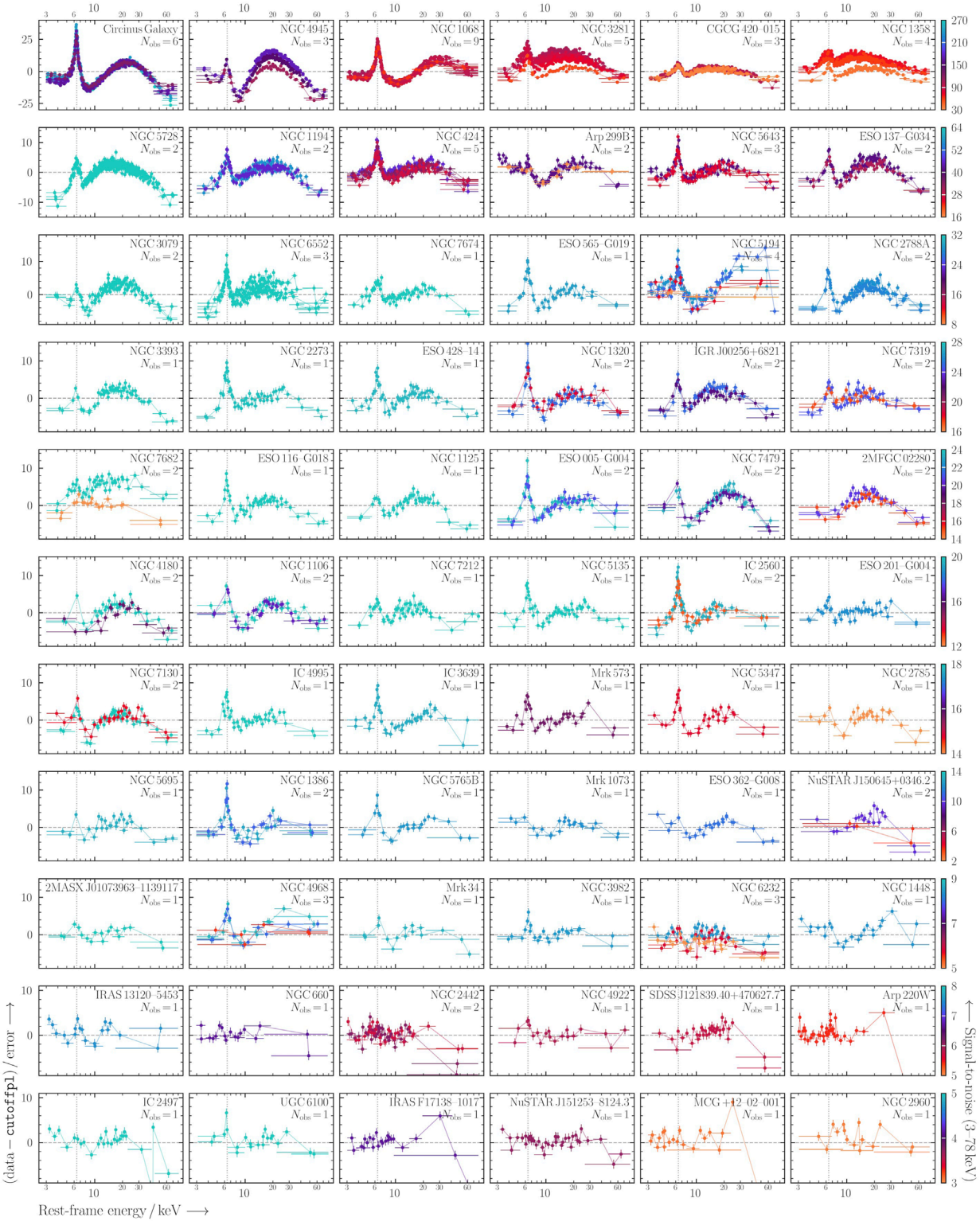

FIGURE 3
Every Compton-thick AGN in DoCTA confirmed by *NuSTAR*: each panel plots the relative residual for a simple `cutoffpl` fit to each *NuSTAR* spectrum with >10 ks of data and is colored by the signal-to-noise ratio in the 3–78 keV band.

3 Developing next-generation models of the circum-nuclear environment

All physical obscurer models feature multiple geometric degrees of freedom that are unique to the geometry assumed (e.g., some combination of line-of-sight column density, global obscurer column density, inclination angle, covering factors, etc.). However, the relative importance for each parameter in a given model fit is often non-trivial with many inter-parameter dependencies and multi-modal solutions to consider. Studies of the obscuration properties of AGN have shown that the covering factor is related to the Eddington-scaled accretion rate (Fabian, 1999; Fabian et al., 2008; Ricci et al., 2017d), meaning that the geometry of the obscurer may be inherently related to the intrinsic properties of the central engine itself. An optimal sample of AGN to observe in X-rays for the development of future obscuration models would hence include 1) Compton-thick obscuration to ensure that the reprocessed emission dominates the observed spectrum, 2) known inclination to remove a geometrical degree of freedom, and 3) precise measurements of black hole mass and multi-wavelength coverage to provide an independent estimate of Eddington-scaled accretion rate.

Disc megamasers satisfy all three criteria. The 22-GHz radio emission line emitted by water vapor is produced by maser amplification[10] and requires highly inclined sight lines to be detected (Zaw et al., 2020). In agreement with the unified model of AGN (Antonucci, 1993; Urry and Padovani, 1995; Netzer, 2015), megamasers are thus often found in Compton-thick AGN in which highly inclined lines-of-sight lead to the highest column densities toward the central engine (Greenhill et al., 2008; Masini et al., 2016; Panessa et al., 2020). Accurate very long baseline interferometry maser mapping additionally provides one of the most precise estimates of the central black hole mass currently known, enabling accurate measurements of Eddington-scaled accretion rate as long as robust bolometric luminosity estimates are available (Brightman et al., 2016). We additionally note that under the unified model, the privileged inclination angles required for 22 GHz water megamaser detection would be purely an orientation effect, with the circum-nuclear obscurer being somewhat similar in all AGN. Thus, future astrophysical surveys of megamasers may be an extremely useful tool not just for studying the circum-nuclear properties of obscured AGN, but the entire AGN population.

In the following sections, we analyze a sample of confirmed Compton-thick AGN with detected water megamaser emission as a basis for developing the next generation of physically motivated obscuration models for *HEX-P*.

3.1 *NuSTAR*-confirmed Compton-thick megamasers

As a basis for our simulations, we selected a sample of 10 Compton-thick AGN in DoCTA with confirmed 22 GHz megamaser in the literature (Masini et al., 2016; Panessa et al., 2020). We additionally included NGC 2960 from Masini et al. (2016) since the target was one of the lowest signal-to-noise ratio sources in their analysis, providing an interesting comparison for *HEX-P*. The sample considered is shown in Table 1. To ensure accurate spectral simulations, we then complemented the longest *NuSTAR* exposure available per source with the *Chandra* observation that was closest in time to the *NuSTAR* observation. Each *Chandra* observation was reprocessed using the `chandra_repro` command in `CIAO` (Fruscione et al., 2006), before creating circular source + background and annular background-only regions centered on the target with each level 2 event file. Owing to the poorer angular resolution of *NuSTAR* compared to *Chandra*, we additionally created circular source + background regions for all clearly visible off-nuclear sources that were within the *NuSTAR* extraction region. Spectra and response files were then produced using the `specextract` command. The breakdown of the sample in terms of source properties and X-ray observations are shown in Table 1. The level of flux contaminating the *NuSTAR* spectra from extracted off-nuclear sources was found to be negligible compared to all AGN apart from NGC 5643. The source has a well-studied ultraluminous X-ray source that has to be accounted for in our spectral analysis (Annuar et al., 2015). We note that at a separation of ~ 50", the AGN and ultraluminous X-ray source would be easily resolved by both the HET and LET onboard *HEX-P* (see Section 5.1).

For X-ray spectral fitting, we use BXA v2.9 that connects the PyMultiNest nested sampling algorithm (Feroz et al., 2009; Buchner et al., 2014) to PyXspec (Gordon and Arnaud, 2021), the Python wrapper for the X-ray spectral fitting environment `Xspec` (Arnaud, 1996). We chose to fit each AGN component with the `UXCLUMPY` model and its associated omnidirectional Thomson scattered emission table. Since we primarily require a good enough description of the observed *Chandra* + *NuSTAR* spectra to perform *HEX-P* simulations, we did not test additional physically motivated models. `UXCLUMPY` does, however, include two unique geometrical parameters that describe the covering factor of material in the obscurer: `TORsigma`, the angular dispersion of the cloud distribution, and `CTKcover`, the covering factor of an additional inner ring of Compton-thick clouds surrounding the AGN. Our spectral model for the AGN in `Xspec` parlance is as follows:

$$\begin{aligned}\text{AGN Model} = {} & \overbrace{\texttt{constant}}^{\text{Cross-calibration}} \times \overbrace{\texttt{TBabs}}^{\text{Galactic absorption}} \\ & \times \Big[\overbrace{\texttt{apec}}^{\text{Thermal}} + \overbrace{\texttt{uxclumpy\_cutoff\_transmit}}^{\text{Transmitted emission}} \\ & + \overbrace{\texttt{uxclumpy\_cutoff\_reflect}}^{\text{Reprocessed emission}} + \overbrace{\texttt{constant}}^{\text{Scattered fraction}} \\ & \times \underbrace{\texttt{uxclumpy\_cutoff\_omni}}_{\text{Warm mirror emission}} \Big]. \end{aligned} \tag{1}$$

For the ultraluminous X-ray source in NGC 5643, we additionally include the following model:

$$\begin{aligned}\text{ULX Model} = {} & \overbrace{\texttt{constant}}^{\text{Contamination factor}} \times \overbrace{\texttt{TBabs}}^{\text{Galactic absorption}} \\ & \times \Big[\overbrace{\texttt{zTBabs}}^{\text{Intrinsic absorption}} \times \overbrace{\texttt{zcutoffpl}}^{\text{Hard X-ray power-law}} + \overbrace{\texttt{diskpbb}}^{\text{Thermal emission}} \Big]. \end{aligned} \tag{2}$$

We assumed non-informative priors for line-of-sight column density, intrinsic power-law exponential cutoff, intrinsic power-law normalization, the omnidirectional scattered fraction, Compton-thick inner ring covering factor, cosine of the obscurer dispersion,

10 The name megamaser is assigned to sources with 22 GHz luminosities in excess of 10 $L_{\odot}$.

TABLE 1 Megamaser sample properties and X-ray observations used in this work.

Name (1)	z (2)	D Mpc (3)	Type (4)	M_{BH} 10^6 $M_\odot$ (5)	Ref. (6)	Obs. ID *NuSTAR* (7)	T/ks *NuSTAR* (8)	Obs. ID *Chandra* (9)	T/ks *Chandra* (10)
IC 2560	0.00976	32.9	i	3.5 ± 0.5	1	50001039004	49.6	4908	55.7
NGC 1194	0.01360	61.3	z	65 ± 3	2	60501011002	58.3	22881	21.1
NGC 1386	0.00290	16.2	i	$1.2^{+1.1}_{-0.6}$	3	60201024002	26.4	13257	34.3
NGC 2273	0.00614	30.3	i	7.5 ± 0.4	2	60001064002	23.2	19377	10.1
NGC 2960	0.01650	92.5	i	11.6 ± 0.5	2	60001069002	20.7	22270	10.1
NGC 3079	0.00369	17.6	i	$2.4^{+2.4}_{-1.2}$	3	60662004002	24.6	20947	45.1
NGC 3393	0.01250	56.3	z	31 ± 2	4	60061205002	15.7	13968	28.5
NGC 5643	0.00400	10.5	i	—	—	60061362006	48.1	17664	42.1
NGC 5728	0.00932	27.9	i	—	—	60662002002	24.9	23254	20.1
NGC 7479	0.00792	25.2	i	—	—	60061316002	23.6	10120	10.2

Notes. (1)—Galaxy identifier. (2)—Spectroscopic redshift. (3)—Distance in Mpc. (4)—Distance type: i = redshift-independent, z = redshift dependent. (5)—Black hole mass in 10^6 $M_\odot$ derived exclusively from megamaser emission. (6)—Black hole mass reference: 1: Yamauchi et al. (2012), 2: Kuo et al. (2011), 3: McConnell and Ma (2013), 4: Kondratko et al. (2008). (7)—*NuSTAR*, observation ID. (8)—*NuSTAR*/FPMA, exposure time in ks. (9)—*Chandra* observation ID. (10)—*Chandra* exposure time in ks.

thermal soft–excess temperature, and its associated normalization. For the intrinsic power-law photon index, we assumed a Gaussian prior with mean 1.8 and standard deviation 0.15 in agreement with numerous X-ray surveys (Ricci et al., 2017c). Finally, for cross-calibrations between *Chandra* and FPMB relative to FPMA, we assumed log-Gaussian priors with mean 0 and standard deviation 0.03, consistent with the values of Madsen et al. (2015). In total, there were 11 free parameters in the UXCLUMPY AGN model.

We find all sources to have column densities in excess of 10^{24} cm^{-2} to 90% confidence. Interestingly, this includes NGC 2960 for which we find a line-of-sight column density solution of $N_H > 1.5 \times 10^{24}$ cm^{-2} to 98.2% confidence by fitting the combined *Chandra* and *NuSTAR* data. Previous works that analyzed the *NuSTAR* data alone consistently found $N_H < 10^{24}$ cm^{-2} using the MYTorus obscuration model (Masini et al., 2016). Due to our Compton-thick solution, we include NGC 2960 in DoCTA *ex post facto*. Figure 3 shows that the *NuSTAR* spectra of NGC 2960 are amongst the lowest signal-to-noise in the 3–78 keV band of all other Compton-thick AGN studied with *NuSTAR* to date. Its low signal-to-noise ratio spectrum thus makes NGC 2960 a challenging and very conservative example to showcase the spectral constraints attainable with *HEX-P*.

3.2 Simulating the faint megamaser NGC 2960

We simulate a grid of *NuSTAR* and *HEX-P* spectra to quantify the relative improvement in physical parameter inference attainable with *HEX-P* observations of NGC 2960. Whilst the Compton-thick solution for NGC 2960 that we report here was acquired with the inclusion of *Chandra* data, we restrict our simulations to purely *NuSTAR* due to the relative scarcity of simultaneous observations publicly available (see Figure 6) and as an extrapolation for the discovery space in hard X-rays of new Compton-thick AGN previously missed. In total, we simulate a range of exposures between 10 ks and 100 ks with 10 realizations per exposure. Each simulated spectrum had the same starting spectrum, namely, the maximum *a posteriori* spectral fit acquired with *Chandra* + *NuSTAR*. However, we additionally set the obscurer dispersion to 60° as this parameter was unconstrained and the Compton-thick inner ring covering factor to 30% since it was only constrained to an approximate upper limit of $\lesssim$ 40% with *NuSTAR*.

The results of the NGC 2960 simulation grid are shown in Figure 4 in terms of 90% posterior parameter constraints on the Eddington ratio (*top panel*) and line-of-sight column density (*bottom panel*) as a function of the exposure time. For Eddington ratio error propagation, we sampled from the black hole mass and associated uncertainties in Table 1. However, for the bolometric correction, we use the Compton-thick bolometric correction from Brightman et al. (2016) of 27.5 that focuses on Compton-thick megamasers. To focus on the improvements attainable purely from X-ray spectral fitting as opposed to other systematics, we assume zero uncertainty on bolometric correction. We justify this choice by assuming the plethora of next-generation multi-wavelength observatories that will be available for quasi-simultaneous observations with *HEX-P* that will provide precise photometric data across the electromagnetic spectrum for accurate measurements of bolometric output. Such observatories include the *James Webb Space Telescope* (Rieke et al. 2015), *Euclid* (Laureijs et al., 2011; Racca et al., 2016), the 4-m multi-object spectroscopic telescope (de Jong et al., 2012), the *Nancy Grace Roman Space Telescope* (Spergel et al., 2015; Akeson et al., 2019), and the Vera C. Rubin Observatory (Ivezić et al., 2019).

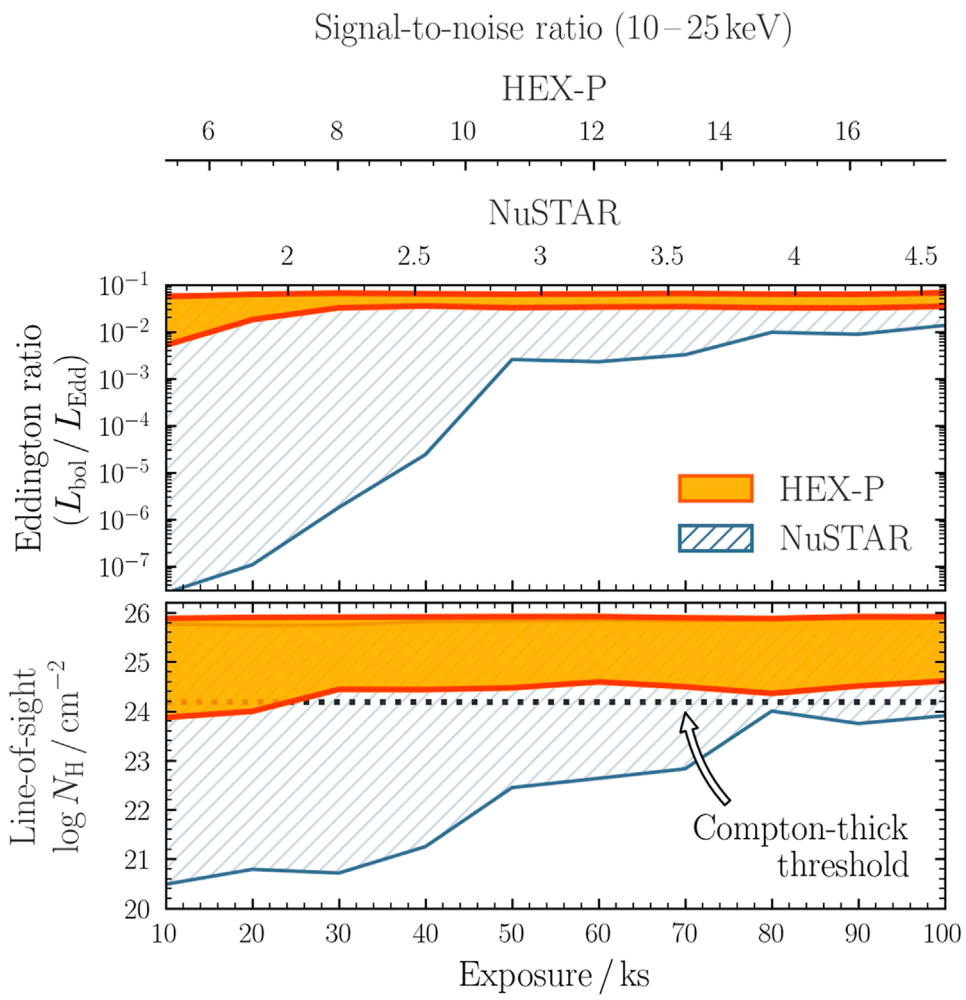

FIGURE 4
Simulated parameter constraints for one of the faintest Compton-thick AGN candidates known: NGC 2960. Bottom panel: Line-of-sight column density posterior 90% quantile range as a function of exposure time for *NuSTAR* (gray hatched region) and *HEX-P* (orange filled region). *HEX-P* could stringently confirm the target as Compton-thick (horizontal dotted line) with a modest ~ 25 ks exposure, which is not possible with *NuSTAR* alone in less than 100 ks Top panel: Same as the bottom one, but for the constrained Eddington ratio. *HEX-P* could constrain the intrinsic luminosity and hence the accretion rate, to comparable precision of the black hole mass for exposures ≳ 30 ks. The top axes show the average measured signal-to-noise ratio in the 10–25 keV band for *NuSTAR* and *HEX-P*, which is found to be ~ 4× higher than that for *NuSTAR* on average.

Even for the low signal-to-noise ratio challenge that NGC 2960 poses, *HEX-P* can achieve Eddington ratio uncertainties comparable to the uncertainties on black hole mass for exposures ≳ 30 ks. By contrast, *NuSTAR* does not reach a similar uncertainty regime for the entire range of exposures considered in the simulations. *HEX-P* can additionally classify the target as Compton-thick to 90% confidence for exposures ≳ 25 ks—a feat that is not possible from purely *NuSTAR* spectroscopy in our simulated range of exposures. We note that the remaining posterior uncertainty above the Compton-thick limit at all exposures with *HEX-P* arises from the stability of the Compton-scattered component in UXCLUMPY. The overall shape of the reprocessed component does not change substantially for line-of-sight column densities $N_H \gtrsim 5 \times 10^{24}$ cm^{-2}, such that constraining line-of-sight column densities to more than a lower limit is currently difficult. The top axis of Figure 4 shows the measured signal-to-noise ratio in the 10–25 keV band for *NuSTAR* and *HEX-P*. The reduced background and simultaneous coverage from three different instruments can boost the signal-to-noise ratio by factors of ~ 4 relative to that of *NuSTAR*. In the case of NGC 2960, the boost in observed signal-to-noise ratio means that a 10-ks exposure with *HEX-P* would require ≫ 100 ks of *NuSTAR* exposure to reach an equivalent 10–25 keV spectral quality. The 10–25 keV energy band holds a plethora of information, not only regarding the line-of-sight column density but also the overall structure of the circum-nuclear obscurer (see Buchner et al., 2019, 2021).

3.3 Prospects for a new era of spectral models

From the signal-to-noise ratio improvements highlighted in Figure 4 and the exceedingly low signal-to-noise ratio of the

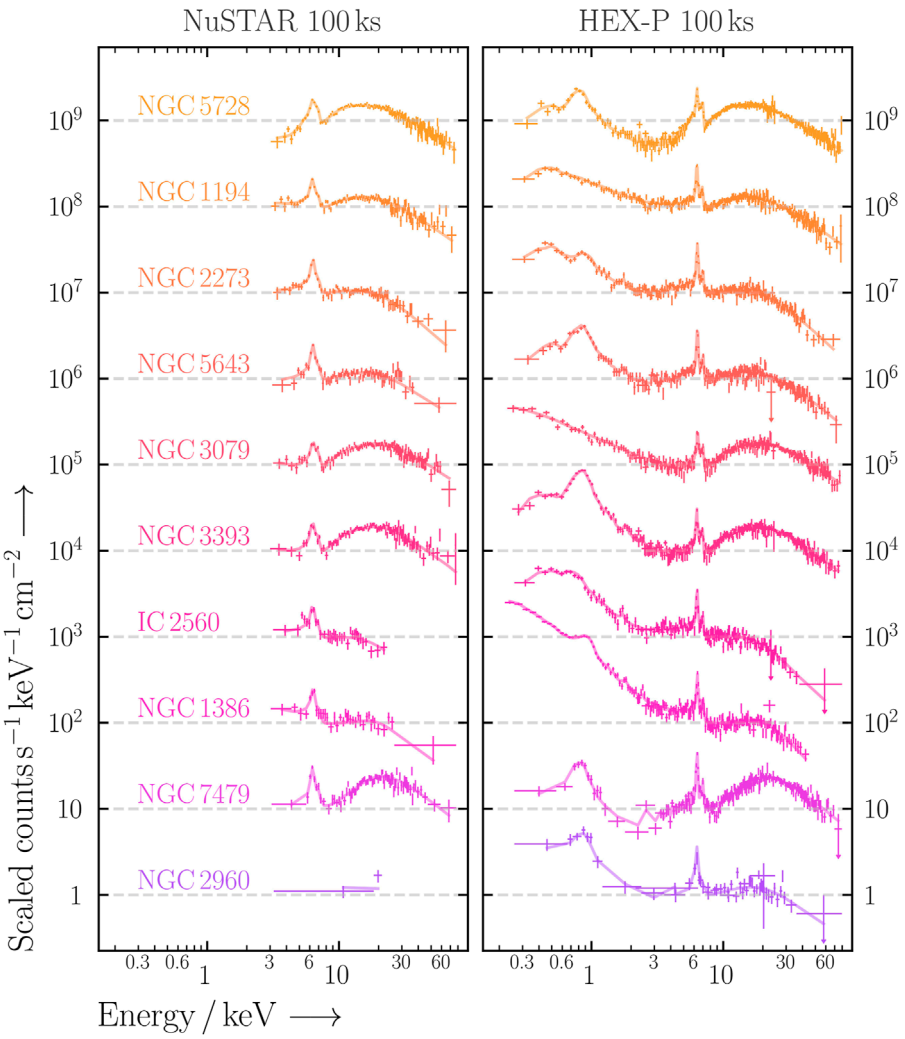

FIGURE 5
Simulating the spectral prospects attainable with *NuSTAR* (*left*) and *HEX-P* (*right*) with 100 ks observations of the Compton-thick megamasers considered in this work. Both panels show the folded simulated spectra from each telescope, normalized by their respective effective areas. *HEX-P* offers a greatly expanded passband, with improved sensitivities up to the highest energies with higher spectral resolution. For each spectrum, any spectral bins with negative lower bounds are shown with The "upper limit arrows" refer to the arrows plotted in the figure that point downwards, and any data that are completely background dominated are omitted for clarity.

NuSTAR data for NGC 2960, it is clear that every known Compton-thick AGN will benefit greatly from modest *HEX-P* observations. Next, we simulate our sample of Compton-thick megamasers for 100 ks with both *NuSTAR* and *HEX-P* to visually showcase the spectral improvements attainable, which will allow the development of next-generation spectral models. In Figure 5, we present a comparison between *NuSTAR* (*left* column) and *HEX-P* (*right* column), ordered from bottom to top by observed 2–10 keV flux. We note that this is already not a like-for-like comparison since *NuSTAR*'s low Earth orbit leads to an ~50% observing efficiency, compared to an ~100% observing efficiency for *HEX-P* observations of $\lesssim 2$ weeks in duration. Despite this, a number of crucial improvements are still visible.

Hard X-ray sensitivity: Whether it be due to the overall spectral slope, high-energy cutoff, structural properties of the obscurer or some combination of each, every AGN has a very distinctive spectral shape >10 keV that is clearly detected with *HEX-P*. By contrast, a large number of the simulated *NuSTAR* spectra are not well detected at $\gtrsim 20$ keV. These improvements offer a number of useful avenues for model constraints and development. Extending the range of detectable energies to $\gtrsim 50$ keV with *HEX-P* will also enable a dramatic reduction in confusion arising from different model components. For example, the high-energy exponential cutoff associated with the intrinsic coronal emission can be extremely difficult to disentangle from the turnover of the Compton hump (Baloković et al., 2019; Kammoun et al., 2023). Furthermore, the covering factor is very dependent on the Compton hump shape, and reducing the measurement uncertainties at $\gtrsim 20$ keV will greatly advance our ability to detect it.

Spectral resolution: From Figure 5, it is clear that the spectral resolution arising from the LET is superior to that of *NuSTAR*.

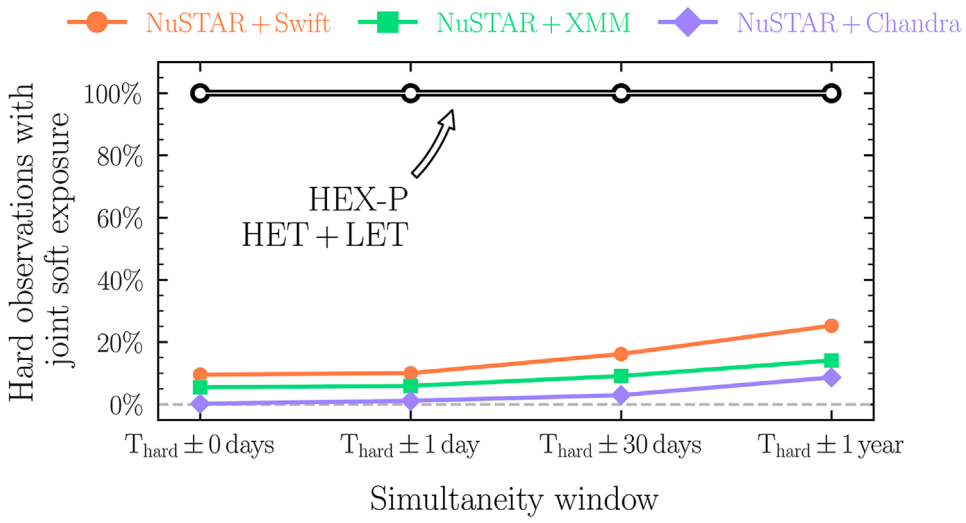

FIGURE 6
Percentage of hard X-ray observations with overlapping soft X-ray exposure available for *NuSTAR* vs. *HEX-P*. To be conservative, in each time window (shown along the horizontal axis), we consider any hard X-ray observation with > 20% of its total exposure overlapping with a soft X-ray observation to be "joint." Archival *NuSTAR* observations were considered for any *Swift*/BAT AGN from the 70-month compilation of Ricci et al. (2017c), obscured with line-of-sight column density $N_H > 10^{22}$ cm^{-2}. Clearly, the complimentary data provided by the LET + HET onboard *HEX-P* will, for the very first time, provide complete simultaneous coverage across the hard and soft X-ray bands.

By combining high spectral resolution measurements of the Fe K region (which includes the Fe Kα and Fe Kβ lines) with sensitive measurements of the underlying reflection continuum up to energies $\gtrsim 20$ keV will enable detailed studies of fluorescence emission in heavily obscured AGN, such as metallicities, dynamics, and emission origins.

Simultaneous soft X-ray coverage: Figure 5 clearly shows the vast range in predicted spectral shapes from our broadband *Chandra* + *NuSTAR* fitting that are not accessible with *NuSTAR*. Whilst quasi-simultaneous soft X-ray coverage is a common strategy for *NuSTAR* observations, exposure times and the corresponding signal-to-noise ratios are often not consistent across instruments (see Figure 6), leading to discrepant measurements of line-of-sight column density (Marchesi et al., 2018). With *HEX-P*, well-matched sensitivities with 100% observing simultaneity will enable broadband X-ray spectral fitting effectively devoid of mismatched signal-to-noise ratio issues.

4 Uncovering the dynamics of the thickest obscurers

Multi-epoch X-ray observations have proven to be a powerful tool for constraining the structure and dynamics of the obscurer. The ability to determine the amount of obscuring material along the line-of-sight as a function of time can be used to place constraints on the sizes of obscuring clumps, as well as their distance from the supermassive black hole (Elvis et al., 2004; Risaliti et al., 2009; Markowitz et al., 2014). Even for sources with sparsely sampled light curves, changes in line-of-sight column densities as a function of time can be used to gain insights into the general scales associated with the obscurer (Laha et al., 2020).

Since the launch of *NuSTAR*, broadband X-ray coverage has allowed the use of complex reflector models, which in turn can constrain global properties of the obscurer such as obscuring covering factor (parameterized as the fraction of sky covered when viewed from the perspective of the corona), inclination angle, and the global obscuring column density out of the line-of-sight (Baloković et al., 2018; Zhao et al., 2019a; Marchesi et al., 2019b; Buchner et al., 2019; Zhao et al., 2019b; Baloković et al., 2021; Zhao et al., 2021). Some works have suggested a correlation between the global properties of the obscurer and the characteristic changes in line-of-sight column densities as a function of the timescale (Pizzetti et al., 2022; Torres-Albà et al., 2023). An advantage of multi-epoch fitting is that parameters unexpected to vary over the relatively short timescales associated with the observations (e.g., the obscurer covering factor or global obscurer column density out of the line-of-sight) can be tied across observing epochs. Such an approach typically leads to more precise constraints on obscurer parameters since there are typically fewer regions of the parameter space compatible with multiple spectra than a single epoch-averaged spectrum (see Baloković et al., 2018; Marchesi et al., 2022; Pizzetti et al., 2022; Torres-Albà et al., 2023).

HEX-P, with its capability to simultaneously observe the soft and hard X-ray bands to greatly improved sensitivity limits, will prove a key instrument for time domain studies (Brightman et al., 2023), such as the time-resolved characterization AGN obscuration in X-rays. Non-simultaneous soft and hard band observations impose significant difficulty in disentangling intrinsic coronal luminosity variability from obscuration-related variability. For example, Torres-Albà et al. (2023) found that for up to 7/12 nearby obscured AGN with confirmed long-term X-ray variability, the two variability

options could not be distinguished due to non-simultaneous soft and hard X-ray observations.

With the results of Torres-Albà et al. (2023) in mind, we sought to assess the current availability of multi-epoch broadband X-ray observations amongst the obscured AGN population. We queried the High-Energy Astrophysics Science Archive Research Center[11] for targeted *NuSTAR* observations of any AGN in the 70-month BAT catalog with line-of-sight column densities $N_{\rm H} > 10^{22}$ cm^{-2}, according to the X-ray spectral fitting catalogs of Ricci et al. (2017c). We then searched for soft X-ray coverage from *XMM-Newton*, *Swift*/XRT, or *Chandra* for each of the 372 obscured AGN with available *NuSTAR* observations (439 *NuSTAR* observations in total). Figure 6 quantifies the frequency of joint soft + *NuSTAR* observations in the obscured AGN sample as a function of ever-increasing hard X-ray observation simultaneity window. To be conservative, we consider any *NuSTAR* observation with > 20% of its total exposure with joint soft exposure within each considered time window to be 'joint'. Even by liberally considering the non-simultaneous scenario of soft observations within 1 year of the *NuSTAR* observations, only ~ 25% have > 20% of their exposure coincident with *NuSTAR* exposure. Even though almost every *NuSTAR* observation considered should have a quasi-simultaneous short (~1–2 ks) *Swift*/XRT coordinated observation, the XRT exposures are typically far shorter than each corresponding *NuSTAR* observation. Having considerably different *NuSTAR* and soft X-ray exposure times can give rise to dramatically different data quality across the spectral passband. Data quality mismatches have been shown to influence measurements of obscuration parameters in heavily obscured AGN considerably (Marchesi et al., 2018; Tanimoto et al., 2022. *HEX-P* will clearly revolutionize the field, providing 100% strictly simultaneous broadband coverage for all observations.

In the sections that follow, we quantify the advances *HEX-P* will make toward multi-epoch observations of obscured AGN with detailed simulations.

4.1 Case study I: non-Compton-thick obscured AGN

First, we consider an obscured but not Compton-thick AGN (line-of-sight $N_{\rm H} \lesssim 10^{24}$ cm^{-2}) that presents both intrinsic luminosity and line-of-sight obscuration variability over three epochs of observation. To make our simulations conservative, we normalize the source flux to NGC 835—the faintest AGN in the sample of Torres-Albà et al. (2023) with confirmed line-of-sight column density variability. We parameterize the obscurer with the `borus02` model (Baloković et al., 2018) in the decoupled mode, in which the obscurer properties were tuned to match the properties derived by Zhao et al. (2021) for a sample of ~ 100 obscured AGN. We simulate and fit with the same model to avoid any systematic uncertainties associated with the *a priori* unknown obscurer that could be more dramatic for the less sensitive *NuSTAR* data than *HEX-P* (i.e., fewer model spectra can accommodate a given *HEX-P* spectrum than *NuSTAR* with reduced sensitivities and passband; see Saha et al., 2022). We consider three different line-of-sight column densities, namely, $N_{\rm H} = 1, 3, 6 \times 10^{23}$ cm^{-2}. To model additional flux variability, we include a cross-normalization constant to the intrinsic AGN emission to simulate 50%, 100%, and 200% flux variability for each of the three observational epochs, respectively. We pair line-of-sight column densities with different flux variability constant values per observational epoch to show increased intrinsic flux with increased line-of-sight column density. We then run spectral simulations of 20 ks exposure times with *NuSTAR* and *HEX-P* before refitting to quantitatively compare each mission's ability to disentangle the two separate forms of variability we consider.

Figure 7 shows the results of our simulations. The *left* panel presents the simulated *HEX-P* spectra, in which the variations in column density from the photoelectric turnover and intrinsic flux from the overall normalizations are clearly visible. The *right* panel shows the resulting constraints in terms of intrinsic flux and line-of-sight column density for both *HEX-P* and the equivalent simulated *NuSTAR* spectra. Overall, we find uncertainties ~ 3–4 times larger with *NuSTAR* than with *HEX-P*. We additionally find the *NuSTAR* constraints on line-of-sight column density to be systematically lower than for *HEX-P*, likely caused by the difficulties associated with constraining the photoelectric turnover purely from a passband above 3 keV. The *NuSTAR* constraints can only place upper limits on the lowest line-of-sight column density scenario that we considered, primarily due to its lack of simultaneous soft band coverage encompassing the photoelectric turnover at soft energies. At higher column densities, the remaining two scenarios are consistent within 99% confidence in terms of both line-of-sight column density constraints and intrinsic flux. By contrast, even for a short 20 ks snapshot, *HEX-P* has no issue in disentangling intrinsic flux variability from line-of-sight column density variability for the full range of column densities considered. The broader passband is crucial, enabling proper characterization of obscuration changes visible through the photoelectric turnover that are degenerate with intrinsic flux changes at harder energies.

4.2 Case study II: Compton-thick AGN

As discussed in Section 1, there have been comparatively few detailed multi-epoch broadband spectroscopic studies of Compton-thick AGN to date, which are dominated by the brightest sources known (Puccetti et al., 2014; Marinucci et al., 2016). An additional limitation with observing variability in Compton-thick AGN is that eclipsing events or intrinsic flux variations are more likely to manifest at ≳10 keV, where the effects of photoelectric absorption are reduced and Compton scattering dominates providing excess detectable flux (Marinucci et al., 2016; Zaino et al., 2020). The improved sensitivity at >10 keV with *HEX-P* will lead to new insights into broadband variability characteristics of Compton-thick AGN that have not been possible to date. To simulate the prospects attainable with *HEX-P*, we use the faintest Compton-thick AGN with a published multi-epoch *NuSTAR*-based campaign to date as the baseline. The nearby Seyfert 2 galaxy NGC 1358 (z = 0.0134) was subjected to a multi-epoch monitoring campaign with *NuSTAR* and *XMM-Newton* between 2017 and 2022 and was found to be highly variable in line-of-sight column density by Marchesi et al. (2022).

11 https://heasarc.gsfc.nasa.gov

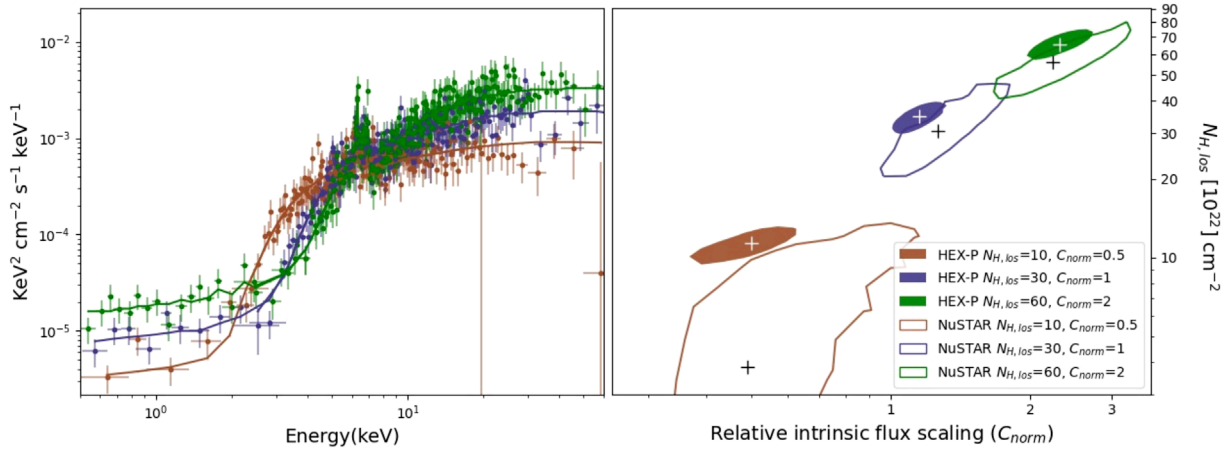

FIGURE 7
Left panel: *HEX-P*/LET + HET spectra simulated with 20 ks exposures from the model described in Section 4.1, based on NGC 835 as a baseline. Colors correspond to the different combinations of line-of-sight column density and intrinsic flux scaling. *Right* panel: Corresponding 99% confidence contours between intrinsic flux scaling vs. line-of-sight column density derived from *HEX-P* (filled) and *NuSTAR* (empty). The crosses represent the best-fit values.

For our *HEX-P* simulations, we use decoupled `borus02` and choose a range of line-of-sight column densities consistent with those measured for NGC 1358 by Marchesi et al. (2022) that varied above and below the Compton-thick limit in a changing-look behavior. The specific line-of-sight column densities that we considered were $N_{\rm H}$ = 0.8, 1.4, 2×10^{24} cm^{-2}. To make our simulations applicable to the wider AGN population, we choose a value of Γ = 1.8, consistent with the broader population of low-redshift Seyfert galaxies (Ricci et al., 2017c). The Thomson-scattered flux fraction is set to 2%, which is again conservative, considering the latest relationships between scattered fraction and line-of-sight column density from Gupta et al. (2021). We additionally include a thermal `apec` component (with temperature kT = 0.3 keV) to model the remaining soft excess flux that the Thomson-scattered power-law does not account for. The global obscuring column density out of the line-of-sight is assumed to be $N_{\rm H} = 3.2\times10^{23}$ cm^{-2} with a covering factor of 15% within the `borus02` model.

The intrinsic 2–10 keV luminosity of NGC 1358 was found by Marchesi et al. (2022) to be $L_{2-10\ \rm keV}$ ~6–9 × 10^{42} erg s^{-1} with a corresponding observed 2–10 keV flux $F_{2-10\ \rm keV}$ = 4–12 × 10^{-13} erg s^{-1} cm^{-2}. To understand the new parameter space that *HEX-P* will probe, we simulate a fiducial source more than an order of magnitude fainter than NGC 1358 with $L_{2-10\ \rm keV}$ = 5 × 10^{41} erg s^{-1}, corresponding to the observed fluxes of $F_{2-10\ \rm keV}$ = 11, 6, 4 × 10^{-14} erg s^{-1} cm^{-2} for each line-of-sight column density considered. We note that equivalent fluxes (and hence spectroscopic constraints) would be constrained for a target at 10 times the distance of NGC 1358 (i.e., D ~500–600 Mpc) with Seyfert-like luminosities of $L_{2-10\ \rm keV}$ ~ 5 × 10^{43} erg s^{-1}. In comparison, it is currently very difficult to perform detailed X-ray spectroscopic modeling of Seyfert-luminosity Compton-thick AGN with *NuSTAR* at comparable distances (Giman et al., 2023).

We simulate one 30-ks *HEX-P* observation for each line-of-sight column density state mentioned above. The line-of-sight column density is recovered to high accuracy with relative uncertainties ≤20%. Owing to the strong advantage of linking parameters that are not expected to vary between epochs, the global column density is precisely recovered with uncertainties < 0.3 dex, and the obscuration covering factor is correctly found to be < 20% to high confidence. Our simulations thus clearly show that a *HEX-P* monitoring campaign would allow us to characterize the properties of the clumpy obscuring medium in heavily obscured AGN with unprecedented quality to far fainter flux levels than are attainable with current X-ray observatories. Such capabilities are critical for constraining the dynamics of the obscurer in the wider Compton-thick AGN population that is currently impossible.

5 The circum-nuclear obscurer of AGN at low accretion power

Our knowledge of the obscurer surrounding low-accretion-power AGN is currently severely incomplete. A root cause is the considerable challenge to select and classify true low-accretion-power AGN, especially at high line-of-sight column densities. *NuSTAR* has provided an unprecedented view into the hard X-ray properties of the circum-nuclear environment of low-luminosity AGN for the first time (Ursini et al., 2015; Annuar et al., 2017; Young et al., 2018; Younes et al., 2019; Annuar et al., 2020; Diaz et al., 2020; Baloković et al., 2021; Diaz et al., 2023). *NuSTAR* has also led to the discovery and classification of a few low-luminosity Compton-thick AGN (Annuar et al., 2017; Brightman et al., 2018; Da Silva et al., 2021), providing exciting evidence that suggests AGN can sustain a significant obscuration structure at low luminosities. However, current observational studies of Compton-thick low-luminosity AGN are often hindered by the requirement for deep integration times to obtain sufficient counts for detailed X-ray spectral modeling (Annuar et al., 2020).

Given the current scarcity of *bona fide* low-luminosity Compton-thick AGN confirmed by broadband X-ray studies that

include hard X-ray observations with *NuSTAR*, we sought to investigate the prospects attainable with *HEX-P* for identifying, classifying, and studying this elusive population in the nearby universe. We tuned our simulations to the properties of four *bona fide* low-luminosity AGN with heavy obscuration in the literature; M51a (Brightman et al., 2018), NGC 660 (Annuar et al., 2020), NGC 1448 (Annuar et al., 2017), and NGC 2442 (Da Silva et al., 2021). We note all sources have column density classifications based in part with *NuSTAR*. In addition, all are confirmed Compton-thick apart from NGC 660 which has both Compton-thick and sub-Compton-thick (but still heavily obscured) solutions in Annuar et al. (2020). With this caveat in mind, for the remainder of this section, we refer to this sample of four sources as the low-luminosity Compton-thick AGN sample.

5.1 Selecting and classifying low-luminosity Compton-thick AGN

A major challenge for studies of low-luminosity AGN is confidently associating detected sources with accretion onto a supermassive black hole, as opposed to off-nuclear accretion onto low-mass compact objects such as ultraluminous X-ray sources, other individual X-ray binaries, or jetted emission (see Bachetti et al., 2023; Lehmer et al., 2023; Connors et al., 2023; Marcotulli et al., 2023 for the *HEX-P* perspective on ultraluminous X-ray sources, other extragalactic accreting compact objects, and resolved AGN jets). A major advantage arises from spectral coverage at $\gtrsim 10$ keV in which the spectral curvature from accreting supermassive black holes can be dramatically different from that of low-mass accreting compact objects. However, an additional difficulty with classification is being able to resolve emission components into individual sources to confidently ascertain the spectral parameters of the central AGN. Given the dramatic improvement in X-ray angular resolution of *HEX-P* compared to both *XMM-Newton* and *NuSTAR*, we sought to test *HEX-P*'s ability to resolve contaminating sources in the host galaxy from low-luminosity AGN.

We base our simulations on the central region of M 51 which is known to host a Compton-thick low-luminosity AGN and a number of bright off-nuclear X-ray sources (Brightman et al., 2018). Our main consideration here was "ULX-3," which is situated ~ 30" from the central AGN and is the closest spatial contamination of all four sources in the Compton-thick low-luminosity AGN sample. Though spatially resolved with *Chandra*, the close separation led to strong contamination with *NuSTAR* that must be accounted for by simultaneously fitting both data sets to infer spectral parameters of the central AGN and ULX-3.

To demonstrate *HEX-P*'s unique capability to spatially resolve closely separated sources in both the soft and hard X-ray energy bands, we compare current constraints from *Chandra* and *NuSTAR* to that of *HEX-P* with simulations. We simulate *HEX-P* soft (<10 keV) and hard (>10 keV) X-ray imaging of M51a and the nearby ultraluminous X-ray source (ULX-3, Brightman et al., 2018) using the Simulated Observations of X-ray Sources (SOXS, ZuHone et al., 2023) and Simulation of X-ray Telescopes (SIXTE, Dauser et al., 2019) software suites. We rely upon SOXS for creating SIMulated inPUT (SIMPUT) files, which incorporates our spectral and spatial models for individual targets. For simplicity, we choose all emission to have energies > 2 keV, in order to exclude any softer extended X-ray emission from the simulation and to enable a more direct study of the resolving power of *HEX-P*.

We use point source models to simulate the spatial morphology of M51a and ULX-3. For spectral modeling, we fit the *Chandra* spectra for M51a and ULX-3 simultaneously with the unresolved *NuSTAR* spectrum of both sources using the same UXCLUMPY-based model described in Section 3 combined with the ultraluminous X-ray source model used to fit NGC 5643. We allow the AGN model to vary for the M51a *Chandra* spectrum and combine the *NuSTAR* spectrum and *vice versa* for ULX-3. The individual AGN and ULX-3 maximum *a posteriori* models found with BXA were then used in conjunction with the spatial model to generate a SIMPUT file. Next, we use SIXTE to produce the telescope event files, energy-filtered imaging, and spectroscopic data products. In order to compare *HEX-P*'s capabilities with current facilities, we also use archival event files for *Chandra*/ACIS-S (0.1–8 keV) and *NuSTAR*/FPMA + FPMB (3–78 keV).

We show the simulated *HEX-P*/LET and HET imaging in Figure 8, juxtaposed with the simulated *Chandra* and *NuSTAR* imaging of the same sources. Despite resolving the AGN and ultraluminous X-ray source well, *Chandra* could only study the targets below 8 keV. As discussed throughout this paper, this limitation considerably restricts the ability for physical inference of the obscurer. It is also clear from the figure that while *NuSTAR* has access to soft (< 10 keV) and hard (> 10 keV) X-ray energies, it cannot spatially resolve the X-ray sources well on these spatial scales. *HEX-P* provides a unique combination of high spatial resolution *broadband* observations, enabling a new era of spatially resolved closely separated nuclear sources. These simulations showcase the power and complementary nature of *HEX-P*/LET and HET imaging to provide enhanced searches of heavily obscured low-luminosity AGN in our nearby galactic neighborhood.

5.2 The nature of the obscurer at low accretion powers

The covering factor of the obscurer at low accretion powers is currently very uncertain, due in part to the difficulty associated with selecting heavily obscured low-luminosity AGN relative to their less obscured counterparts. Here, we investigate the ability of *HEX-P* to study the covering factor of Compton-thick AGN via detailed spectral modeling of individual sources.

To provide a firm basis for our simulations, we begin from all archival *Chandra* and *NuSTAR* data available for NGC 660, NGC 2442, and NGC 1448. For NGC 2442, there were two archival *NuSTAR* and two archival *Chandra* observations. We extracted the spectra following the same criteria as throughout this paper, before manually checking for significant variability between observations. Due to the lack of strong variability, we then co-added all *NuSTAR*/FPMA, *NuSTAR*/FPMB, and *Chandra* spectra individually to provide ~49.5 ks of total *Chandra* exposure and ~ 112 ks of *NuSTAR* exposure. For NGC 1448 and NGC 660, we extracted the *Chandra* and *NuSTAR* data following the methods from Annuar et al. (2017) and Annuar et al. (2020),

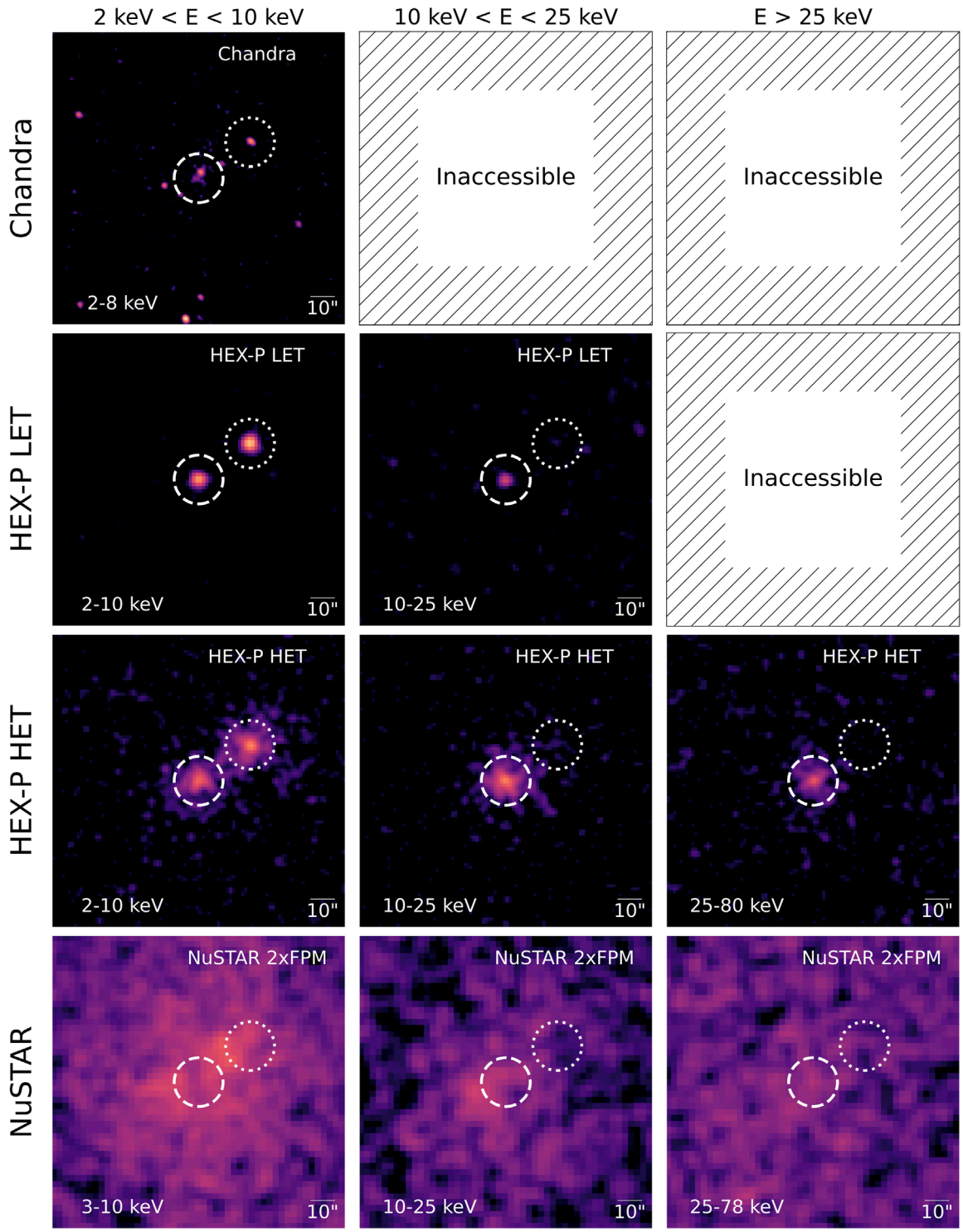

FIGURE 8
Comparing the energy coverage and spatial resolution of *Chandra*, *NuSTAR*, and *HEX-P* for the case of M51a and the nearby ULX-3. The rows represent *Chandra*, *HEX-P*/LET, *HEX-P*/HET, and *NuSTAR*, from top to bottom. The columns represent increasing energy bands, with *left* showing 2 keV < *E* <10 keV; *middle*, 10 keV < *E* <25 keV; and *right*, *E* >25 keV. For instruments without access to a specific energy passband, the panel is marked as "inaccessible." All tiles are centered on M51a (dashed circle) and the off-center source is ULX-3 (dotted circle). Clearly, *Chandra* can spatially resolve M51a and ULX-3 but does not have access to harder X-ray energies (>10 keV). By contrast, *NuSTAR* has broadband coverage (3 – 78 keV), but lacks the angular resolution to resolve the two sources. *HEX-P* will provide spatially resolved measurements of M51a and ULX-3 in both the 2–25 keV passband with the LET and the 2–80 keV passband with the HET. The half-power diameters are 3.5″ for the LET and 10″, 17″, and 23″ at 10, 30, and 60 keV, respectively, for the HET.

respectively. We additionally included the same absorbed power-law model components from Annuar et al. (2017) for two off-nuclear contaminants inevitably included in the NGC 1448 *NuSTAR* extraction region that were resolved by *Chandra*. The two contaminant model components were kept frozen to their best-fit values from Annuar et al. (2017) for all fitting that involved *NuSTAR*. However, given the results of Section 5.1, *HEX-P* could easily resolve these contaminants from the AGN such that any spectral simulations and corresponding fitting of *HEX-P* spectra only considered the AGN component in NGC 1448.

We then performed spectral modeling using the UXCLUMPY model (Buchner et al., 2019), which included emission from a clumpy obscurer, soft X-ray excess emission from an omnipresent warm mirror, and a thermal component with apec. We experimented with a number of spectral fitting setups, but due to the low signal-to-noise ratio of the observed spectra, a number of unphysical parameter constraints had to be avoided. One example is the tendency for the fit to prefer a low covering-factor obscurer (i.e., the TORsigma parameter in UXCLUMPY tended toward its minimum) in exchange for a hard X-ray photon index and overall unobscured spectrum. Similar degeneracies are well documented in the literature (Brightman et al., 2015), and as such, we opted to freeze TORsigma to a fiducial value of 60° for the spectral fitting of archival data.

Interestingly, the resulting parameter posteriors indicated a diversity in CTKcover between sources, suggesting a diversity in Compton hump shapes across the three sources fit here[12]. From each acquired modal posterior model spectrum, we simulated the corresponding *HEX-P*/LET and *HEX-P*/HET spectra with 100 ks exposures before re-running the same spectral fits with TORsigma additionally left free to vary. Given the distribution of column densities assigned to clouds in the UXCLUMPY model (Buchner et al., 2019), it is difficult to parametrically calculate a covering factor for a particular cloud configuration. We instead used pre-tabulated calculations of covering factor for all material with $N_{\rm H} > 10^{22}$ cm^{-2} and $N_{\rm H} > 10^{24}$ cm^{-2} for a two-dimensional grid of TORsigma and CTKcover values. We used grid interpolation to propagate all posterior uncertainties from TORsigma and CTKcover into posteriors for both of these column density regimes.

To investigate *HEX-P*'s ability to probe the precise relationships between accretion power and covering factor in Compton-thick low-luminosity AGN, we required an estimate of the Eddington ratio for each target. The black hole masses that we used were $\log M_{\rm BH}/M_{\odot} = 7.35 \pm 0.50$ (Annuar et al., 2020)[13], 7.28 ± 0.33 (Davis et al., 2014), and $6.0^{+0.1}_{-0.5}$ (Annuar et al., 2017) for NGC 660, NGC 2442, and NGC 1448, respectively. We then used the bolometric correction relationship shown in Eq. (2) of Nemmen et al. (2014) for low-luminosity AGN to estimate the posterior distribution on the bolometric correction.

The corresponding two-dimensional contours shown in Figure 9 give the posteriors on the Eddington ratio vs. covering factor for material with $N_{\rm H} > 10^{22}$ cm^{-2} and $N_{\rm H} > 10^{24}$ cm^{-2} in the *left* and *right* panels, respectively. Both covering factors are calculated from the Supplementary Appendix Table 2 in Section 8, which lists the spherically averaged angle covering factors above two column densities. *HEX-P* spectroscopy can thus constrain the covering factor to within $\lesssim$20% in the lowest luminosity Compton-thick AGN currently known. Such observations are critical to understand the presence and corresponding importance of circum-nuclear obscuration in the low-luminosity regime.

6 An intermediate mass black hole confirmed with megamaser emission

To explore the parameter space attainable with *HEX-P* in the search for obscured intermediate mass black holes, we start from the work of Chen et al. (2017) who selected a sample of 10 low-mass AGN from the 40-month *NuSTAR* serendipitous survey. Of this sample, IC 750 has a confirmed 22 GHz water megamaser signature (Zaw et al., 2020), placing a tight upper bound on the central black hole mass in the intermediate mass range of $M_{\rm BH} < 1.4 \times 10^5$ M$_{\odot}$. As discussed in Section 3, megamasers are ideal targets for *HEX-P* to aid the development of future circum-nuclear obscuration models, and hence IC 750 provides an extension to the black hole mass range of known megamaser AGN. Furthermore, Chen et al. (2017) performed phenomenological X-ray spectral fitting to an ~30 ks *Chandra* spectrum of IC 750, finding the source to be heavily obscured with line-of-sight $N_{\rm H} \sim 1.2 \times 10^{23}$ cm^{-2}. As discussed by Chen et al. (2017) and throughout this work, X-ray spectral fitting to a predominantly soft band spectrum without sensitive broadband coverage can give rise to wide systematic uncertainties on the properties of the obscurer.

We downloaded and reprocessed all archival *Chandra* data sets of IC 750 using the chandra_repro command available in CIAO (Fruscione et al., 2006). The level 2 event files were then used to create the circular source + background and annular background-only regions centered on the target. We made sure to make the source + background regions small enough to remove as much contamination as possible from the $E < 2$ keV diffuse extended emission reported by Chen et al. (2017). The background regions were created to be as large as possible whilst avoiding off-nuclear sources and chip gaps. Source + background, background, and response spectral files were then produced using the specextract command.

After a variety of different tests of significant spectral variability, we chose to co-add the six individual X-ray spectra using the ftool command addspec. The resulting co-added spectrum contained a net exposure of 177 ks with 441 source counts detected in the 0.5–8 keV band (see the *left* panel of Figure 10). As an initial assessment of the spectrum, we fit a similar model to Chen et al. (2017), namely, an absorbed power-law with an additional thermal component provided by apec and a narrow Gaussian line to represent the Fe K complex. The corresponding folded spectrum with shaded posterior and two-dimensional posterior between observed 0.5–8 keV luminosity and Fe K equivalent width are shown

12 The clouds that form the inner ring described by CTKcover in UXCLUMPY are assigned log $N_{\rm H}$ drawn from a log-normal distribution with $N_{\rm H} = 10^{25.5 \pm 0.5}$ cm^{-2}.

13 We conservatively assumed 0.5 dex uncertainty for NGC 660 when propagating uncertainties on the Eddington ratio posterior.

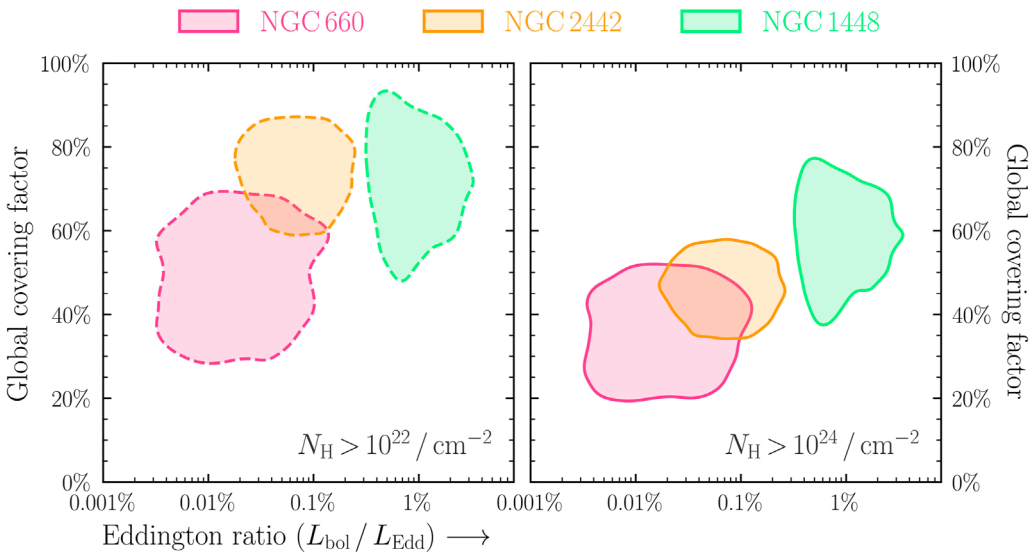

FIGURE 9
HEX-P 100 ks simulation contours for *NuSTAR*-confirmed low-luminosity Compton-thick AGN. The posterior contours show Eddington ratio vs. covering factor for material in the UXCLUMPY geometry with *left:* $N_H > 10^{22}$ cm^{-2} and *right:* $N_H > 10^{24}$ cm^{-2}. Note: due to the overall similar correlations between TORsigma, CTKcover, and the global covering factors of material with $N_H > 10^{22}$ cm^{-2} and $N_H > 10^{24}$ cm^{-2} (see Section 8), the propagated uncertainties in global covering factor have similar shapes. Performing similar spectral fitting to archival *NuSTAR* + *Chandra* data was insufficient to break degeneracies associated with the covering factor, photon index, and line-of-sight column density—see Section 5.2 for details. For both panels, the contours encompass 90% of the probability.

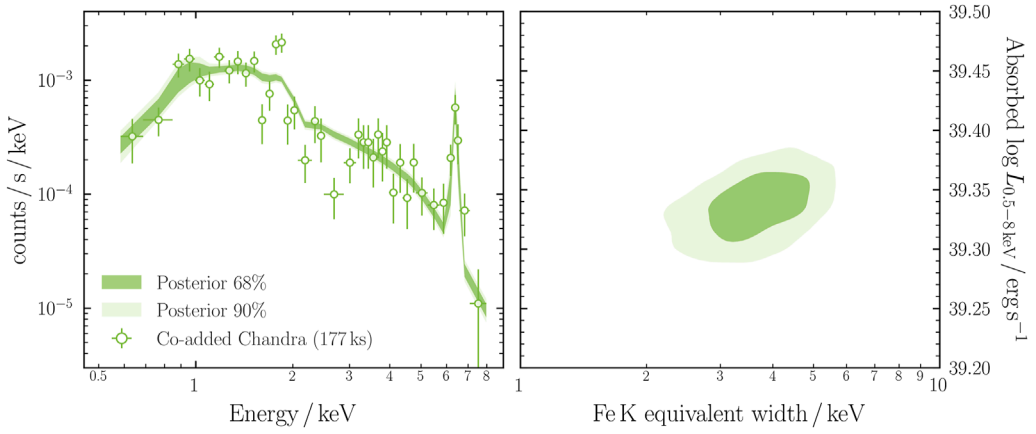

FIGURE 10
(*Left*) Co-added *Chandra* spectrum of IC 750, fit with a phenomenological model. (*Right*) Posterior 2D contour between observed 0.5–8 keV luminosity and Fe K equivalent width derived from the spectral fit shown in the *left* panel.

in the *left* and *right* panels of Figure 10, respectively. Despite the observed (i.e., absorption uncorrected) 0.5–8 keV luminosity being consistent with ultraluminous X-ray sources (Earnshaw et al., 2019), the observed Fe K equivalent width is enormous with a value of > 2 keV at > 99% confidence. The probability of such large equivalent widths to occur in lower obscuration AGN or off-nuclear ultraluminous X-ray sources is virtually impossible. Such high equivalent widths are even rare for Compton-thick AGN, though not unheard of (see Levenson et al., 2002; Boorman et al., 2018), and strongly indicate a deeply buried accreting massive black hole.

6.1 Inferring the obscuration geometry with *HEX-P*

To provide a basis for *HEX-P* simulations, we next turned to physically motivated spectral models of obscuration. To test the distinguishing power of broadband X-ray spectroscopy, we fit the existing co-added *Chandra* spectrum with two distinctive physical X-ray obscuration models: BNsphere (Brightman and Nandra, 2011a), representing a spherical distribution of matter, and UXCLUMPY (Buchner et al., 2019), representing a clumpy distribution of matter. Despite using the BNsphere model, we

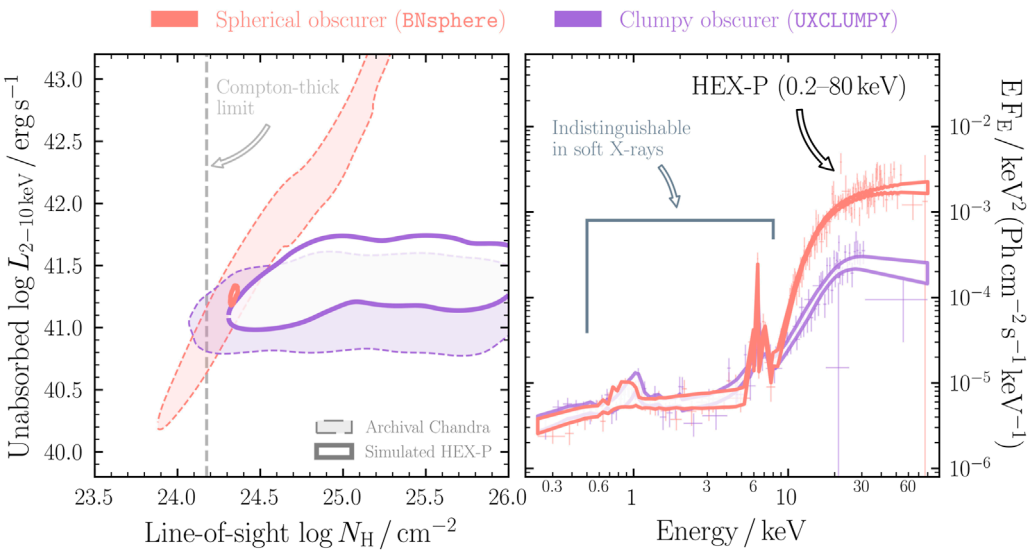

FIGURE 11
(*Left*) Posterior 2D contours between intrinsic 2–10 keV luminosity and line-of-sight column density derived with the BNsphere and UXCLUMPY physically motivated obscuration models. The posterior contours derived from fitting the archival *Chandra* data are shown with light shading bounded by a dashed line. The constraints from fitting simulated *HEX-P* spectra are shown with transparent white contours bounded by thick lines. *HEX-P* can easily constrain the target to be Compton-thick with high confidence and precisely measure the intrinsic luminosity of the buried X-ray corona. (*Right*) Simulated *HEX-P* spectra with posterior range derived from spectral fitting. The soft X-ray band covered by archival *Chandra* spectroscopy is insufficient to distinguish spectral models. By contrast, the broad passband of *HEX-P* encompasses stark spectral differences in the Compton hump, enabling geometrical constraints on the obscurer. Both panels show posterior ranges encompassing 99% probability.

include a soft X-ray excess component in both model fits that is often attributed to a small fraction of intrinsic X-ray fluxes escaping through less-obscured sight-lines. Though unlikely in a spherical model (i.e., there are no less-obscured sight-lines when surrounded by fully covering obscuration), by allowing a small amount of fluxes to escape, we approximately reproduce a leaky-sphere geometry akin to that described in Greenwell et al. (2022). Some contribution to the soft X-ray excess in obscured AGN may still come from larger scales than the circum-nuclear obscurer (see discussion in Gupta et al., 2021), such that our approximation is justified. Both physically motivated obscurer model setups are assumed to be coupled (i.e., the line-of-sight obscuration is assumed to be the same as the global obscuration level out of the line-of-sight).

The line-of-sight column density vs. intrinsic luminosity posterior distributions from the spectral fits to the existing *Chandra* data are shown in the *left* panel of Figure 11 with light shading, encompassed by a dashed line. BNsphere and UXCLUMPY found IC 750 to have line-of-sight column density in excess of the Compton-thick limit to ~85% and ~99% probability[14], making IC 750 a firm Compton-thick accreting intermediate mass black hole candidate.

However, as shown in the *right* panel of Figure 11, the existing soft band *Chandra* spectral coverage is incapable of distinguishing the two obscuration models. This means that the true range of the intrinsic luminosity posterior that we have derived from the spectral fitting spans ~4 dex, and the properties of the obscurer cannot be constrained (see LaMassa et al., 2017, 2019 for more discussion on this). We next simulate *HEX-P*/LET and HET spectra from the modal posterior parameter values derived by fitting the *Chandra* data, using exactly the same exposure as the co-added *Chandra* spectrum for both models and re-fit with BXA. The resulting posterior contours and simulated spectra unfolded with the best-fitting model posteriors are shown with transparent white contours encompassed by thick borders in the *left* and *right* panels of Figure 11, respectively. Clearly the broadband coverage provided by *HEX-P* could dramatically decrease the luminosity degeneracy of the BNsphere model fit, as well as definitively constrain the line-of-sight column density as Compton-thick. The dramatic difference between the two model fits in the *right* panel at energies > 10 keV is crucial since *HEX-P* can not only precisely measure intrinsic luminosities and line-of-sight column densities but also distinguish between obscuration geometries.

HEX-P is hence well poised to find, classify, and study obscured accretion onto intermediate mass black holes. Gaining access to spectroscopic information of sufficient sensitivity at > 10 keV is additionally crucial to decipher genuine intermediate mass black hole accretion from other lower mass compact object accretion in the host galaxy.

7 The discovery space for Compton-thick AGN

The Compton-thick population remains extremely elusive and uncertain, not just in X-ray surveys of the distant universe but even in our nearest cosmic volumes < 100 Mpc (Ricci et al.,

14 We note that the BNsphere posterior gives a >99% probability for a line-of-sight column density in excess of 10^{24} cm^{-2}.

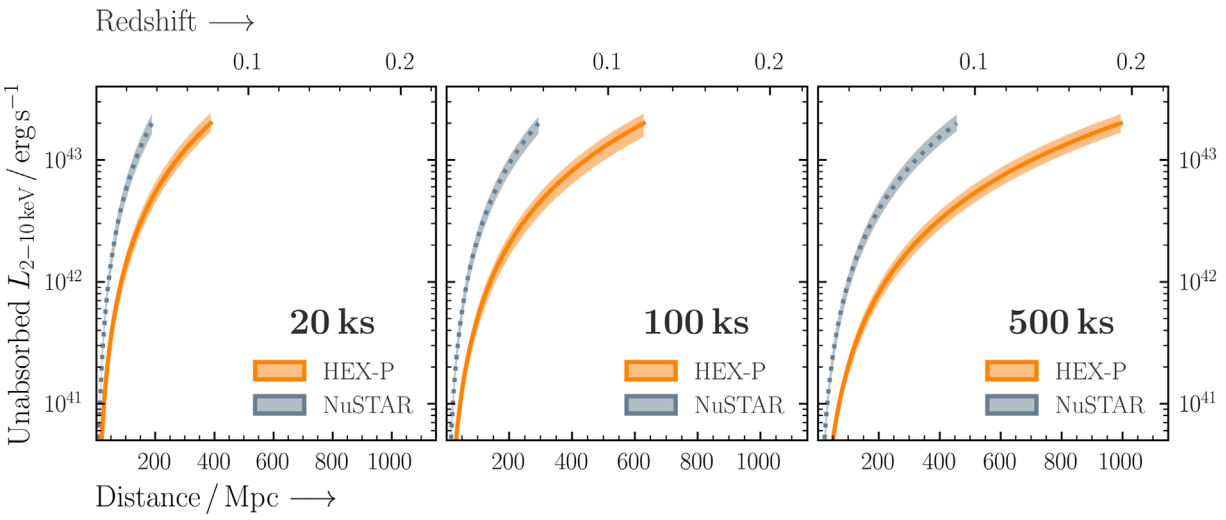

FIGURE 12
Sensitivity curves with 90% probability ranges for the discovery and detailed study of Compton-thick AGN in hard X-rays. *Left*, *center*, and *right* panels correspond to exposure times of 20 ks, 100 ks, and 500 ks, respectively. Across all panels, each curve shows the combination of distance (horizontal axis) and unabsorbed X-ray luminosity in the 2–10 keV band (vertical axis) that gives an observed signal-to-noise ratio of 8 in the hard 10–25 keV band. The simulations detailed in Figure 4 show that this requirement on signal-to-noise is sufficient to correctly classify an AGN as Compton-thick to 90% confidence. By increasing the volume for discovery and detailed study by an order of magnitude relative to *NuSTAR*, *HEX-P* will open up a new era in the pursuit of a complete AGN census.

2015; Asmus et al., 2020; Torres-Albà et al., 2021). A big open question is the volume for which we can reliably classify AGN as Compton-thick and whether the spectral data are sufficient to constrain the morphology of the circum-nuclear obscurer. Here, we demonstrate the much larger search volume accessible with *HEX-P* than *NuSTAR* for the detailed study of Compton-thick AGN.

We build upon the simulations of NGC 2960 detailed in Section 3.2 and shown in Figure 4 and characterize the luminosity and distance space that can be accessed with a given exposure time. We created a large grid of spectral simulations for a Compton-thick AGN UXCLUMPY model with line-of-sight column density $N_{\mathrm{H}} = 1.5 \times 10^{24}$ cm^{-2} and a ∼50% covering factor of material with $N_{\mathrm{H}} > 10^{22}$ cm^{-2}. We simulate spectra with 20 ks, 100 ks, and 500 ks exposures for a grid of distance and unabsorbed 2–10 keV luminosities. For each grid point, we generate 10 realizations to estimate the scatter arising from statistical fluctuations. For each exposure time and each luminosity, we identify the distance out to which line-of-sight column densities $N_{\mathrm{H}} < 1.5 \times 10^{24}$ cm^{-2} can be ruled out to 90% significance based on the 10–25 keV signal-to-noise ratio (as per Figure 4).

HEX-P will double the distance out to which Compton-thick AGN can be securely discovered, over what was possible with *NuSTAR*. This is demonstrated in Figure 12, in three separate panels for the considered exposure times. Each panel plots the unabsorbed 2–10 keV luminosity as a function of distance. We note that for Compton-thick column densities, the corresponding observed 2–10 keV luminosities would be ∼1 – 2 dex lower, dependent upon the choice of spectral model. We choose a fiducial unabsorbed 2–10 keV luminosity of 2×10^{43} erg s^{-1} to define the limiting distance for Compton-thick AGN classifications in our simulations. Figure 12 shows that irrespective of exposure time, *HEX-P* can provide detailed spectral classifications of Compton-thick AGN to ≳2× the distance of *NuSTAR*, increasing the available volume and number of target sources by ∼8–10×. Even for the shortest exposure considered of 20 ks, *HEX-P* would provide full characterization of the Compton-thick AGN population with unabsorbed 2–10 keV luminosities $L_{2-10\ \mathrm{keV}} > 10^{42}$ erg s^{-1} within 100 Mpc. This encompasses the current volume cut of the highly complete multi-wavelength selected Local AGN Survey that predicts 362^{+145}_{-116} AGN within the volume with 61 AGN previously unidentified (LASr; Asmus et al., 2020).

For very long exposures ≳300 ks, the effective volume for sensitive *HEX-P* spectral modeling of the Compton-thick population extends to ∼1 Gpc for Seyfert-luminosity AGN with unabsorbed 2–10 keV luminosities $L_{2-10\ \mathrm{keV}} \gtrsim 10^{43}$ erg s^{-1}. The corresponding large accessible volume for detailed spectral modeling is testament to the vast jump in sensitivity provided by *HEX-P*. This will be pivotal in probing the dusty hearts of galaxies such as mergers, ultra/luminous infrared galaxies, and compact obscured nuclei that have been suggested to host deeply buried Compton-thick AGN (Iwasawa et al., 2011; Torres-Albà et al., 2018; Aalto et al., 2019; Ricci et al., 2021; Falstad et al., 2021; Pfeifle et al., 2023. Together with the planned *HEX-P* extragalactic surveys (Civano et al., 2023) and a wide array of multi-wavelength facilities, detailed studies of Compton-thick AGN will pave the way toward a complete census of black hole growth across cosmic time.

8 Summary

In this paper, we detail many aspects of heavily obscured AGN studies performed in the literature to date with an extrapolation to the prospects attainable with the next-generation *HEX-P* concept.

We begin by compiling an up-to-date and highly complete catalog of Compton-thick AGN confirmed with spectroscopic fitting that incorporated *NuSTAR* (DoCTA; see Section 2). We show that there is an enormous range of measured line-of-sight column density and intrinsic luminosity for the targets, highlighting the requirement for improved broadband spectroscopy paired with next-generation multi-wavelength models of the circum-nuclear obscurer.

The key findings from our *HEX-P* simulations are as follows:

- *The development of future AGN models with HEX-P:* With the findings of DoCTA in mind, we present an analysis of archival *NuSTAR* + *Chandra* data for 10 Compton-thick megamaser AGN. Megamasers have some of the best constrained black hole masses with known inclinations that would help create physically motivated models of the obscurer that depend on accretion power. We showcase *HEX-P* simulations for the faintest megamaser in our sample, finding that an exposure of 25 ks suffices to classify the target as Compton-thick to better than 90% confidence and to measure the intrinsic accretion rate precisely.
- *Strictly simultaneous broadband X-ray spectroscopy: HEX-P* will provide highly sensitive and strictly simultaneous X-ray spectroscopic observations in the 0.2–80 keV passband for the first time. We show that future *HEX-P* monitoring campaigns of heavily obscured AGN will disentangle obscuration-based variations from intrinsic flux variations to much greater precision than is possible with current instruments.
- *The nature of the circum-nuclear environment at low accretion power:* It is currently extremely difficult to constrain the geometry of circum-nuclear obscuration at low intrinsic AGN power. We show that the enhanced sensitivities and angular resolution of *HEX-P* are essential for 1) disentangling true low-luminosity AGN from off-nuclear compact objects and 2) constraining the covering factor of the obscurer in sources with $L_{\rm bol} \lesssim 10^{42}$ erg s^{-1}.
- *The obscured growth of intermediate mass black holes:* Current estimates of the black hole occupation fraction rely on the detection of dwarf AGN that are biased toward unobscured sources. We show detailed *HEX-P* simulations of one candidate Compton-thick intermediate mass AGN in the literature. We show that sensitive broadband spectroscopy from *HEX-P* is sufficient to not only constrain the line-of-sight column density into the Compton-thick regime but also differentiate between alternative physical prescriptions for the geometry of the obscurer.
- *A new discovery space for Compton-thick AGN:* We determine the accessible volume for accurate characterization of Compton-thick AGN. We find the improved sensitivities provided by *HEX-P* will more than double the distance and increase the accessible volume by up to an order of magnitude relative to *NuSTAR*.

Data availability statement

Publicly available data sets were analyzed in this study. These data can be found at https://heasarc.gsfc.nasa.gov/cgi-bin/W3Browse/w3browse.pl.

Author contributions

PB: conceptualization, data curation, formal analysis, investigation, methodology, project administration, supervision, validation, visualization, writing—original draft, and writing–review and editing. NT-A: conceptualization, formal analysis, validation, visualization, writing—original draft, and writing–review and editing. AA: conceptualization, data curation, formal analysis, investigation, writing–original draft, and writing–review and editing. SM: conceptualization, data curation, formal analysis, investigation, writing–original draft, and writing–review and editing. RP: conceptualization, data curation, formal analysis, investigation, visualization, writing–original draft, and writing–review and editing. DSt: conceptualization and writing–review and editing. FC: conceptualization, and writing–review and editing. MBa: conceptualization, and writing–review and editing. JB: conceptualization, writing–original draft, and writing–review and editing. CR: conceptualization and writing–review and editing. DA: writing–review and editing. WB: conceptualization and writing–review and editing. MBr: writing–review and editing. CC: conceptualization and writing–review and editing. SC: writing–review and editing. PG: conceptualization and writing–review and editing. JG: conceptualization and writing–review and editing. FH: writing–review and editing. RH: conceptualization, writing–review and editing. EK: writing–review and editing. SL: writing–review and editing. GL: writing–review and editing. LM: writing–review and editing. KM: writing–review and editing. G. Matt: writing–review and editing. GM: writing–review and editing. EN: conceptualization and writing–review and editing. JP: writing–review and editing. AP: writing–review and editing. SP: writing–review and editing. DSi: writing–review and editing. RS: writing–review and editing. DJW: writing–review and editing. DRW: writing–review and editing. XZ: conceptualization and writing–review and editing.

Funding

The author(s) declare that financial support was received for the research, authorship, and/or publication of this article. The work of DS was carried out at the Jet Propulsion Laboratory, California Institute of Technology, under a contract with NASA. NT-A acknowledges funding from NASA under contracts 80NSSC19K0531, 80NSSC20K0045, and 80NSSC20K834. RP gratefully acknowledges support through an appointment to the NASA Postdoctoral Program at Goddard Space Flight Center, administered by ORAU through a contract with NASA. JP acknowledges support from NASA grants 80NSSC21K1567 and 80NSSC22K1120. MBa acknowledges support from the YCAA Prize Postdoctoral Fellowship. CR acknowledges support from the Fondecyt Regular grant 1230345 and ANID BASAL project FB210003.

Acknowledgments

The authors thank both referees for their constructive feedback and comments that helped improve the clarity of the paper. PB

would like to additionally thank Abhijeet Borkar for their useful comments and discussions related to the megamaser section of the manuscript. This work made use of data from the NuSTAR mission, a project led by the California Institute of Technology, managed by the Jet Propulsion Laboratory, and funded by the National Aeronautics and Space Administration. We thank the NuSTAR Operations, Software and Calibration teams for support with the execution and analysis of these observations. This research has made use of the NuSTAR Data Analysis Software (NuSTARDAS) jointly developed by the ASI Science Data Center (ASDC, Italy) and the California Institute of Technology (USA). This research has made use of data obtained from the Chandra Data Archive and the Chandra Source Catalog, and software provided by the Chandra X-ray Center (CXC) in the application packages CIAO and Sherpa. This research has made use of the NASA/IPAC Extragalactic Database (NED), which is operated by the Jet Propulsion Laboratory, California Institute of Technology, under contract with the National Aeronautics and Space Administration. This research has made use of NASA's Astrophysics Data System Bibliographic Services. This work made use of Astropy:[15] a community-developed core Python package and an ecosystem of tools and resources for astronomy (Astropy Collaboration et al., 2013; Astropy Collaboration, 2018; Astropy Collaboration, 2022). This paper made extensive use of the matplotlib (Hunter, 2007), Scipy (Virtanen et al., 2020) and Pandas (McKinney, 2010) Python packages.

Conflict of interest

The authors declare that the research was conducted in the absence of any commercial or financial relationships that could be construed as a potential conflict of interest.

The author(s) declared that they were an editorial board member of Frontiers, at the time of submission. This had no impact on the peer review process and the final decision.

Publisher's note

Supplementary material

The Supplementary Material for this article can be found online at: https://www.frontiersin.org/articles/10.3389/fspas.2024.1335459/full#supplementary-material

References

Aalto, S., Muller, S., König, S., Falstad, N., Mangum, J., Sakamoto, K., et al. (2019). The hidden heart of the luminous infrared galaxy IC 860. I. A molecular inflow feeding opaque, extreme nuclear activity. *A&A* 627, A147. doi:10.1051/0004-6361/201935480

Aird, J., Coil, A. L., Georgakakis, A., Nandra, K., Barro, G., and Pérez-González, P. G. (2015). The evolution of the X-ray luminosity functions of unabsorbed and absorbed AGNs out to z ~ 5. *MNRAS* 451, 1892–1927. doi:10.1093/mnras/stv1062

Akeson, R., Armus, L., Bachelet, E., Bailey, V., Bartusek, L., Bellini, A., et al. (2019). *The wide field infrared survey telescope: 100 hubbles for the 2020s. arXiv e-prints* , arXiv:1902.05569. doi:10.48550/arXiv.1902.05569

Akylas, A., Georgakakis, A., Georgantopoulos, I., Brightman, M., and Nandra, K. (2012). Constraining the fraction of Compton-thick AGN in the Universe by modelling the diffuse X-ray background spectrum. *A&A* 546, A98. doi:10.1051/0004-6361/201219387

Ananna, T. T., Treister, E., Urry, C. M., Ricci, C., Kirkpatrick, A., LaMassa, S., et al. (2019). The accretion history of AGNs. I. Supermassive black hole population synthesis model. *ApJ* 871, 240. doi:10.3847/1538-4357/aafb77

Ananna, T. T., Urry, C. M., Ricci, C., Natarajan, P., Hickox, R. C., Trakhtenbrot, B., et al. (2022). Probing the structure and evolution of BASS active galactic nuclei through Eddington ratios. *ApJ* 939, L13. doi:10.3847/2041-8213/ac9979

Andonie, C., Alexander, D. M., Greenwell, C., Puglisi, A., Laloux, B., Alonso-Tetilla, A. V., et al. (2023). Obscuration beyond the nucleus: infrared quasars can be buried in extreme compact starbursts. *MNRAS* 527, L144–L150. doi:10.1093/mnrasl/slad144

Andonie, C., Ricci, C., Paltani, S., Arévalo, P., Treister, E., Bauer, F., et al. (2022). A multiwavelength-motivated X-ray model for the Circinus Galaxy. *MNRAS* 511, 5768–5781. doi:10.1093/mnras/stac403

Anglés-Alcázar, D., Quataert, E., Hopkins, P. F., Somerville, R. S., Hayward, C. C., Faucher-Giguère, C.-A., et al. (2021). Cosmological simulations of quasar fueling to subparsec scales using Lagrangian hyper-refinement. *ApJ* 917, 53. doi:10.3847/1538-4357/ac09e8

Annuar, A., Alexander, D. M., Gandhi, P., Lansbury, G. B., Asmus, D., Ballantyne, D. R., et al. (2017). A new compton-thick AGN in our cosmic backyard: unveiling the buried nucleus in NGC 1448 with NuSTAR. *ApJ* 836, 165. doi:10.3847/1538-4357/836/2/165

Annuar, A., Gandhi, P., Alexander, D. M., Anathpindika, S., Asmus, D., Ballantyne, D. R., et al. (2020). A deep x-ray view of the bare agn ark120. v. spin determination from disc-comptonisation efficiency method. *Mon. Notices R. Astronomical Soc.* 492, 5481–5500. doi:10.1093/mnras/staa205

Annuar, A., Gandhi, P., Alexander, D. M., Lansbury, G. B., Arévalo, P., Ballantyne, D. R., et al. (2015). NuSTAR observations of the compton-thick active galactic nucleus and ultraluminous X-ray source candidate in NGC 5643. *ApJ* 815, 36. doi:10.1088/0004-637X/815/1/36

Ansh, S., Chen, C.-T. J., Brandt, W. N., Hood, C. E., Kammoun, E. S., Lansbury, G., et al. (2023). NuSTAR observations of a heavily X-ray-obscured AGN in the dwarf galaxy J144013+024744. *ApJ* 942, 82. doi:10.3847/1538-4357/ac9382

Antonucci, R. (1993). Unified models for active galactic nuclei and quasars. *ARA&A* 31, 473–521. doi:10.1146/annurev.aa.31.090193.002353

Arévalo, P., Bauer, F. E., Puccetti, S., Walton, D. J., Koss, M., Boggs, S. E., et al. (2014). The 2-79 keV X-ray spectrum of the Circinus galaxy with NuSTAR, xmm-Newton, and chandra: a fully compton-thick active galactic nucleus. *ApJ* 791, 81. doi:10.1088/0004-637X/791/2/81

Arnaud, K. A. (1996). "XSPEC: the first ten years," in *Astronomical data analysis software and systems V*. Editors G. H. Jacoby, and J. Barnes (Astronomical Society of the Pacific), 17.

Asmus, D., Greenwell, C. L., Gandhi, P., Boorman, P. G., Aird, J., Alexander, D. M., et al. (2020). Local AGN survey (LASr): I. Galaxy sample, infrared colour selection, and predictions for AGN within 100 Mpc. *MNRAS* 494, 1784–1816. doi:10.1093/mnras/staa766

Astropy Collaboration, Robitaille, T. P., Tollerud, E. J., Greenfield, P., Droettboom, M., Bray, E., et al. (2013). Astropy: a community Python package for astronomy. *A&A* 558, A33. doi:10.1051/0004-6361/201322068

Astropy Collaboration, Price-Whelan, A. M., Sipőcz, B. M., Günther, H. M., Lim, P. L., Crawford, S. M., et al. (2018). The Astropy project: building an open-science project and status of the v2.0 core package. *AJ* 156, 123. doi:10.3847/1538-3881/aabc4f

15 http://www.astropy.org

Astropy Collaboration, Price-Whelan, A. M., Lim, P. L., Earl, N., Starkman, N., Bradley, L., et al. (2022). The Astropy project: sustaining and growing a community-oriented open-source project and the latest major release (v5.0) of the core package. *ApJ* 935, 167. doi:10.3847/1538-4357/ac7c74

Bachetti, M., Middleton, M. J., Pinto, C., Gúrpide, A., Walton, D. J., Brightman, M., et al. (2023). *The high energy X-ray probe (HEX-P): studying extreme accretion with ultraluminous X-ray sources. arXiv e-prints* , arXiv:2311.04733. doi:10.48550/arXiv.2311.04733

Baldassare, V. F., Geha, M., and Greene, J. (2018). Identifying AGNs in low-mass galaxies via long-term optical variability. *ApJ* 868, 152. doi:10.3847/1538-4357/aae6cf

Baldi, R. D., Williams, D. R. A., Beswick, R. J., McHardy, I., Dullo, B. T., Knapen, J. H., et al. (2021a). LeMMINGs III. The e-MERLIN legacy survey of the Palomar sample: exploring the origin of nuclear radio emission in active and inactive galaxies through the [O III] - radio connection. *MNRAS* 508, 2019–2038. doi:10.1093/mnras/stab2613

Baldi, R. D., Williams, D. R. A., McHardy, I. M., Beswick, R. J., Argo, M. K., Dullo, B. T., et al. (2018). LeMMINGs - I. The eMERLIN legacy survey of nearby galaxies. 1.5-GHz parsec-scale radio structures and cores. *MNRAS* 476, 3478–3522. doi:10.1093/mnras/sty342

Baldi, R. D., Williams, D. R. A., McHardy, I. M., Beswick, R. J., Brinks, E., Dullo, B. T., et al. (2021b). LeMMINGs - II. The e-MERLIN legacy survey of nearby galaxies. The deepest radio view of the Palomar sample on parsec scale. *MNRAS* 500, 4749–4767. doi:10.1093/mnras/staa3519

Baloković, M. (2017). "Unveiling the structure of active galactic nuclei with hard X-ray spectroscopy,". Ph.D. thesis (California Institute of Technology).

Baloković, M., Brightman, M., Harrison, F. A., Comastri, A., Ricci, C., Buchner, J., et al. (2018). New spectral model for constraining torus covering factors from broadband X-ray spectra of active galactic nuclei. *ApJ* 854, 42. doi:10.3847/1538-4357/aaa7eb

Baloković, M., Cabral, S. E., Brenneman, L., and Urry, C. M. (2021). Properties of the obscuring torus in NGC 1052 from multiepoch broadband X-ray spectroscopy. *ApJ* 916, 90. doi:10.3847/1538-4357/abff4d

Baloković, M., Comastri, A., Harrison, F. A., Alexander, D. M., Ballantyne, D. R., Bauer, F. E., et al. (2014). The NuSTAR view of nearby compton-thick active galactic nuclei: the cases of NGC 424, NGC 1320, and IC 2560. *ApJ* 794, 111. doi:10.1088/0004-637X/794/2/111

Baloković, M., García, J. A., and Cabral, S. E. (2019). New tools for self-consistent modeling of the AGN torus and corona. *Res. Notes Am. Astronomical Soc.* 3, 173. doi:10.3847/2515-5172/ab578e

Bañados, E., Venemans, B. P., Mazzucchelli, C., Farina, E. P., Walter, F., Wang, F., et al. (2018). An 800-million-solar-mass black hole in a significantly neutral Universe at a redshift of 7.5. *Nature* 553, 473–476. doi:10.1038/nature25180

Bauer, F. E., Arévalo, P., Walton, D. J., Koss, M. J., Puccetti, S., Gandhi, P., et al. (2015). NuSTAR spectroscopy of multi-component X-ray reflection from NGC 1068. *ApJ* 812, 116. doi:10.1088/0004-637X/812/2/116

Boorman, P. G., Gandhi, P., Alexander, D. M., Annuar, A., Ballantyne, D. R., Bauer, F., et al. (2016). IC 3639—a new *bona fide* compton-thick AGN unveiled by NuSTAR. *ApJ* 833, 245. doi:10.3847/1538-4357/833/2/245

Boorman, P. G., Gandhi, P., Baloković, M., Brightman, M., Harrison, F., Ricci, C., et al. (2018). An Iwasawa-Taniguchi effect for Compton-thick active galactic nuclei. *MNRAS* 477, 3775–3790. doi:10.1093/mnras/sty861

Brandt, W. N., and Alexander, D. M. (2015). Cosmic X-ray surveys of distant active galaxies. The demographics, physics, and ecology of growing supermassive black holes. *A&A Rev.* 23, 1. doi:10.1007/s00159-014-0081-z

Brandt, W. N., and Yang, G. (2022). "Surveys of the cosmic X-ray background," in *Handbook of X-ray and gamma-ray Astrophysics*. Editors C. Bambi, and A. Santangelo (Singapore: Springer Nature), 78. doi:10.1007/978-981-16-4544-0_130-1

Brightman, M., Baloković, M., Stern, D., Arévalo, P., Ballantyne, D. R., Bauer, F. E., et al. (2015). Determining the covering factor of compton-thick active galactic nuclei with NuSTAR. *ApJ* 805, 41. doi:10.1088/0004-637X/805/1/41

Brightman, M., Margutti, R., Polzin, A., Jaodand, A., Hotokezaka, K., Alford, J. A. J., et al. (2023). *The High Energy X-ray Probe (HEX-P): sensitive broadband X-ray observations of transient phenomena in the 2030s. arXiv e-prints* , arXiv:2311.04856. doi:10.48550/arXiv.2311.04856

Brightman, M., Masini, A., Ballantyne, D. R., Baloković, M., Brandt, W. N., Chen, C. T., et al. (2016). A growth-rate indicator for compton-thick active galactic nuclei. *ApJ* 826, 93. doi:10.3847/0004-637X/826/1/93

Brightman, M., Masini, A., Ballantyne, D. R., Baloković, M., Brandt, W. N., Chen, C.-T. J., et al. (2018). Bat agn spectroscopic survey. vii. the covering factor of dust and gas in swift/bat active galactic nuclei. *Astrophysical J.* 867, 110. doi:10.3847/1538-4357/aae4da

Brightman, M., and Nandra, K. (2011a). An XMM-Newton spectral survey of 12 μm selected galaxies - I. X-ray data. *MNRAS* 413, 1206–1235. doi:10.1111/j.1365-2966.2011.18207.x

Brightman, M., and Nandra, K. (2011b). An XMM-Newton spectral survey of 12 μm selected galaxies - II. Implications for AGN selection and unification. *MNRAS* 414, 3084–3104. doi:10.1111/j.1365-2966.2011.18612.x

Buchner, J., and Boorman, P. (2023). *Statistical aspects of X-ray spectral analysis. arXiv e-prints* , arXiv:2309.05705. doi:10.48550/arXiv.2309.05705

Buchner, J., Brightman, M., Baloković, M., Wada, K., Bauer, F. E., and Nandra, K. (2021). Physically motivated X-ray obscurer models. *A&A* 651, A58. doi:10.1051/0004-6361/201834963

Buchner, J., Brightman, M., Nandra, K., Nikutta, R., and Bauer, F. E. (2019). X-ray spectral and eclipsing model of the clumpy obscurer in active galactic nuclei. *A&A* 629, A16. doi:10.1051/0004-6361/201834771

Buchner, J., Georgakakis, A., Nandra, K., Brightman, M., Menzel, M.-L., Liu, Z., et al. (2015). Obscuration-dependent evolution of active galactic nuclei. *ApJ* 802, 89. doi:10.1088/0004-637X/802/2/89

Buchner, J., Georgakakis, A., Nandra, K., Hsu, L., Rangel, C., Brightman, M., et al. (2014). X-ray spectral modelling of the AGN obscuring region in the CDFS: bayesian model selection and catalogue. *A&A* 564, A125. doi:10.1051/0004-6361/201322971

Buchner, J., Schulze, S., and Bauer, F. E. (2017). Galaxy gas as obscurer - I. GRBs x-ray galaxies and find an $N_H{}^3\alpha$ M_{star} relation. *MNRAS* 464, 4545–4566. doi:10.1093/mnras/stw2423

Chan, C.-H., and Krolik, J. H. (2016). Radiation-driven outflows from and radiative support in dusty tori of active galactic nuclei. *ApJ* 825, 67. doi:10.3847/0004-637X/825/1/67

Chen, C. T. J., Brandt, W. N., Reines, A. E., Lansbury, G., Stern, D., Alexander, D. M., et al. (2017). Hard X-ray-selected AGNs in low-mass galaxies from the NuSTAR serendipitous survey. *ApJ* 837, 48. doi:10.3847/1538-4357/aa5d5b

Civano, F., Zhao, X., Boorman, P., Marchesi, S., Ananna, T., Creech, S., et al. (2023). *The high energy X-ray probe (HEX-P): bringing the cosmic X-ray background into focus. arXiv e-prints* , arXiv:2311.04832. doi:10.48550/arXiv.2311.04832

Comastri, A., Gilli, R., Marconi, A., Risaliti, G., and Salvati, M. (2015). Mass without radiation: heavily obscured AGNs, the X-ray background, and the black hole mass density. *A&A* 574, L10. doi:10.1051/0004-6361/201425496

Comastri, A., Setti, G., Zamorani, G., and Hasinger, G. (1995). The contribution of AGNs to the X-ray background. *A&A* 296, 1. doi:10.48550/arXiv.astro-ph/9409067

Connors, R., Tomsick, J., Draghis, P., Coughenour, B., Shaw, A., Garcia, J., et al. (2023). *The high energy X-ray probe (HEX-P): probing accretion onto stellar mass black holes. arXiv e-prints* , arXiv:2311.04782. doi:10.48550/arXiv.2311.04782

Da Silva, R. L., Ricci, C., Sani, E., Koss, M. J., Trakhtenbrot, B., Lamperti, I., et al. (2021). A catalog of low-mass black holes in active galactic nuclei. iv. the catalog content and properties, and constraints on the host galaxies. *Astrophysical J.* 911, 150. doi:10.3847/1538-4357/abec74

Dauser, T., Falkner, S., Lorenz, M., Kirsch, C., Peille, P., Cucchetti, E., et al. (2019). SIXTE: a generic X-ray instrument simulation toolkit. *A&A* 630, A66. doi:10.1051/0004-6361/201935978

Davis, B. L., Berrier, J. C., Johns, L., Shields, D. W., Hartley, M. T., Kennefick, D., et al. (2014). The black hole mass function derived from local spiral galaxies. *ApJ* 789, 124. doi:10.1088/0004-637X/789/2/124

de Jong, R. S., Bellido-Tirado, O., Chiappini, C., Depagne, É., Haynes, R., Johl, D., et al. (2012). "4MOST: 4-metre multi-object spectroscopic telescope," in *Ground-based and airborne instrumentation for astronomy IV*. Editors I. S. McLean, S. K. Ramsay, and H. Takami, 84460T. doi:10.1117/12.926239

Diaz, Y., Arévalo, P., Hernández-García, L., Bassani, L., Malizia, A., González-Martín, O., et al. (2020). Constraining X-ray reflection in the low-luminosity AGN NGC 3718 using NuSTAR and XMM-Newton. *MNRAS* 496, 5399–5413. doi:10.1093/mnras/staa1762

Diaz, Y., Hernàndez-García, L., Arévalo, P., López-Navas, E., Ricci, C., Koss, M., et al. (2023). Constraining the X-ray reflection in low accretion-rate active galactic nuclei using XMM-Newton, NuSTAR, and Swift. *A&A* 669, A114. doi:10.1051/0004-6361/202244678

Earnshaw, H. P., Roberts, T. P., Middleton, M. J., Walton, D. J., and Mateos, S. (2019). A new, clean catalogue of extragalactic non-nuclear X-ray sources in nearby galaxies. *MNRAS* 483, 5554–5573. doi:10.1093/mnras/sty3403

Elitzur, M. (2006). The obscuring torus in AGN. *New Astron. Rev.* 50, 728–731. doi:10.1016/j.newar.2006.06.027

Elitzur, M., and Ho, L. C. (2009). The disk-wind connection in agn: us 322, an interesting case. *Astrophysical J.* 701, L91–L94. doi:10.1088/0004-637X/701/2/L91

Elvis, M., Risaliti, G., Nicastro, F., Miller, J. M., Fiore, F., and Puccetti, S. (2004). An unveiling event in the type 2 active galactic nucleus NGC 4388:A challenge for a parsec-scale absorber. *ApJ* 615, L25–L28. doi:10.1086/424380

Eracleous, M., Hwang, J. A., and Flohic, H. M. L. G. (2010). The narrow-line region of narrow-line and broad-line seyfert 1 galaxies. *Astrophysical J.* 711, 796–811. doi:10.1088/0004-637X/711/2/796

Eraerds, T., Antonelli, V., Davis, C., Hall, D., Hetherington, O., Holland, A., et al. (2021). Enhanced simulations on the athena/wide field imager instrumental background. *J. Astronomical Telesc. Instrum. Syst.* 7, 034001. doi:10.1117/1.JATIS.7.3.034001

Fabian, A. C. (1999). The obscured growth of massive black holes. *MNRAS* 308, L39–L43. doi:10.1046/j.1365-8711.1999.03017.x

Fabian, A. C., Vasudevan, R. V., and Gandhi, P. (2008). The effect of radiation pressure on dusty absorbing gas around active galactic nuclei. *MNRAS* 385, L43–L47. doi:10.1111/j.1745-3933.2008.00430.x

Falstad, N., Aalto, S., König, S., Onishi, K., Muller, S., Gorski, M., et al. (2021). CON-quest. Searching for the most obscured galaxy nuclei. *A&A* 649, A105. doi:10.1051/0004-6361/202039291

Farrah, D., Baloković, M., Stern, D., Harris, K., Kunimoto, M., Walton, D. J., et al. (2016). The geometry of the infrared and X-ray obscurer in a dusty hyperluminous quasar. *ApJ* 831, 76. doi:10.3847/0004-637X/831/1/76

Fernández-Ontiveros, J. A., and Muñoz-Darias, T. (2021). X-ray binary accretion states in active galactic nuclei? Sensing the accretion disc of supermassive black holes with mid-infrared nebular lines. *MNRAS* 504, 5726–5740. doi:10.1093/mnras/stab1108

Feroz, F., Hobson, M. P., and Bridges, M. (2009). MULTINEST: an efficient and robust Bayesian inference tool for cosmology and particle physics. *MNRAS* 398, 1601–1614. doi:10.1111/j.1365-2966.2009.14548.x

Fruscione, A., McDowell, J. C., Allen, G. E., Brickhouse, N. S., Burke, D. J., Davis, J. E., et al. (2006). "CIAO: chandra's data analysis system," in *Society of photo-optical instrumentation engineers (SPIE) conference series*. Editors D. R. Silva, and R. E. Doxsey, 62701V. doi:10.1117/12.671760

Gandhi, P., Annuar, A., Lansbury, G. B., Stern, D., Alexander, D. M., Bauer, F. E., et al. (2017). The weak Fe fluorescence line and long-term X-ray evolution of the Compton-thick active galactic nucleus in NGC 7674. *MNRAS* 467, 4606–4621. doi:10.1093/mnras/stx357

Gandhi, P., and Fabian, A. C. (2003). X-ray background synthesis: the infrared connection. *MNRAS* 339, 1095–1102. doi:10.1046/j.1365-8711.2003.06259.x

Gandhi, P., Fabian, A. C., Suebsuwong, T., Malzac, J., Miniutti, G., and Wilman, R. J. (2007). Constraints on light bending and reflection from the hard X-ray background. *MNRAS* 382, 1005–1018. doi:10.1111/j.1365-2966.2007.12462.x

Gandhi, P., Lansbury, G. B., Alexander, D. M., Stern, D., Arévalo, P., Ballantyne, D. R., et al. (2014). NuSTAR unveils a compton-thick type 2 quasar in mrk 34. *ApJ* 792, 117. doi:10.1088/0004-637X/792/2/117

Gandhi, P., Terashima, Y., Yamada, S., Mushotzky, R. F., Ueda, Y., Baumgartner, W. H., et al. (2013). Reflection-dominated nuclear X-ray emission in the early-type galaxy ESO 565-g019. *ApJ* 773, 51. doi:10.1088/0004-637X/773/1/51

Gandhi, P., Yamada, S., Ricci, C., Asmus, D., Mushotzky, R. F., Ueda, Y., et al. (2015). A Compton-thick AGN in the barred spiral galaxy NGC 4785. *MNRAS* 449, 1845–1855. doi:10.1093/mnras/stv344

Gaspari, M., Brighenti, F., and Temi, P. (2015). Chaotic cold accretion on to black holes in rotating atmospheres. *A&A* 579, A62. doi:10.1051/0004-6361/201526151

Gaspari, M., Ruszkowski, M., and Oh, S. P. (2013). Chaotic cold accretion on to black holes. *MNRAS* 432, 3401–3422. doi:10.1093/mnras/stt692

Gaspari, M., Tombesi, F., and Cappi, M. (2020). Linking macro-meso- and microscales in multiphase AGN feeding and feedback. *Nat. Astron.* 4, 10–13. doi:10.1038/s41550-019-0970-1

Georgantopoulos, I., and Akylas, A. (2019). NuSTAR observations of heavily obscured Swift/BAT AGNs: constraints on the Compton-thick AGNs fraction. *A&A* 621, A28. doi:10.1051/0004-6361/201833038

Gilli, R., Comastri, A., and Hasinger, G. (2007). The synthesis of the cosmic X-ray background in the Chandra and XMM-Newton era. *A&A* 463, 79–96. doi:10.1051/0004-6361:20066334

Gilli, R., Norman, C., Calura, F., Vito, F., Decarli, R., Marchesi, S., et al. (2022). Supermassive black holes at high redshift are expected to be obscured by their massive host galaxies' interstellar medium. *A&A* 666, A17. doi:10.1051/0004-6361/202243708

Giman, A., Boorman, P., Harrison, F., Stern, D., and Baloković, M. (2023). *In prep*. ApJ.

González-Martín, O., Hernández-García, L., Masegosa, J., Marquez, I., and Esquej, P. (2017). A universal scaling for the energetics of relativistic jets from black hole systems. *Astrophysical J.* 835, 16. doi:10.3847/1538-4357/835/1/16

González-Martín, O., Masegosa, J., Márquez, I., Guerrero, M. A., and Dultzin-Hacyan, D. (2009). Unification of x-ray winds in seyfert galaxies: from ultra-fast outflows to warm absorbers. *Mon. Notices R. Astronomical Soc.* 397, L79–L83. doi:10.1111/j.1745-3933.2009.00757.x

Goodman, A. A., Pineda, J. E., and Schnee, S. L. (2009). The "true" column density distribution in star-forming molecular clouds. *ApJ* 692, 91–103. doi:10.1088/0004-637X/692/1/91

Gordon, C., and Arnaud, K. (2021). *PyXspec: Python interface to XSPEC spectral-fitting program*. Astrophysics Source Code Library. record ascl:2101.014.

Greene, J. E. (2012). Low-mass black holes as the remnants of primordial black hole formation. *Nat. Commun.* 3, 1304. doi:10.1038/ncomms2314

Greene, J. E., and Ho, L. C. (2004). Active galactic nuclei with candidate intermediate-mass black holes. *ApJ* 610, 722–736. doi:10.1086/421719

Greene, J. E., and Ho, L. C. (2007). A new sample of low-mass black holes in active galaxies. *ApJ* 670, 92–104. doi:10.1086/522082

Greene, J. E., Strader, J., and Ho, L. C. (2020). Intermediate-mass black holes. *ARA&A* 58, 257–312. doi:10.1146/annurev-astro-032620-021835

Greenhill, L. J., Tilak, A., and Madejski, G. (2008). Prevalence of high X-ray obscuring columns among AGNs that host H_2O masers. *ApJ* 686, L13–L16. doi:10.1086/592782

Greenwell, C., Gandhi, P., Lansbury, G., Boorman, P., Mainieri, V., and Stern, D. (2022). XMM and NuSTAR observations of an optically quiescent quasar. *ApJ* 934, L34. doi:10.3847/2041-8213/ac83a0

Gupta, K. K., Ricci, C., Tortosa, A., Ueda, Y., Kawamuro, T., Koss, M., et al. (2021). BAT AGN Spectroscopic Survey XXVII: scattered X-Ray radiation in obscured active galactic nuclei. *MNRAS* 504, 428–443. doi:10.1093/mnras/stab839

Harrison, F. A., Craig, W. W., Christensen, F. E., Hailey, C. J., Zhang, W. W., Boggs, S. E., et al. (2013). The nuclear spectroscopic telescope array (NuSTAR) high-energy X-ray mission. *ApJ* 770, 103. doi:10.1088/0004-637X/770/2/103

Hernández-García, L., Masegosa, J., González-Martín, O., and Márquez, I. (2016). Subarcsecond imaging of the water maser in ngc 1068 with kvn and vera. *Astrophysical J.* 824, L27. doi:10.3847/2041-8205/824/2/L27

Hickox, R. C., and Alexander, D. M. (2018). Obscured active galactic nuclei. *ARA&A* 56, 625–671. doi:10.1146/annurev-astro-081817-051803

Ho, L. C. (1997). Nuclear activity in nearby galaxies. *Rev. Mex. Astron. Astrofísica* 6, 55–63. doi:10.48550/arXiv.astro-ph/9607118

Ho, L. C. (1999). Narrow-line seyfert 1 galaxies and their place in the universe. *Astrophysical J. Suppl. Ser.* 120, 73–112. doi:10.1086/313181

Ho, L. C. (2008). Nuclear activity in nearby galaxies. *Annu. Rev. Astronomy Astrophysics* 46, 475–539. doi:10.1146/annurev.astro.45.051806.110546

Hönig, S. F., and Beckert, T. (2007). The unified model of active galactic nuclei. *Astrophysical J.* 746, 214–234. doi:10.1088/0004-637X/746/2/214

Hopkins, P. F., Hernquist, L., Cox, T. J., Di Matteo, T., Robertson, B., and Springel, V. (2006). A unified, merger-driven model of the origin of starbursts, quasars, the cosmic X-ray background, supermassive black holes, and galaxy spheroids. *ApJS* 163, 1–49. doi:10.1086/499298

Hunter, J. D. (2007). Matplotlib: a 2d graphics environment. *Comput. Sci. Eng.* 9, 90–95. doi:10.1109/MCSE.2007.55

Ikeda, S., Awaki, H., and Terashima, Y. (2009). Study on X-ray spectra of obscured active galactic nuclei based on Monte Carlo simulation—an interpretation of observed wide-band spectra. *ApJ* 692, 608–617. doi:10.1088/0004-637X/692/1/608

Ivezić, Ž., Kahn, S. M., Tyson, J. A., Abel, B., Acosta, E., Allsman, R., et al. (2019). LSST: from science drivers to reference design and anticipated data products. *ApJ* 873, 111. doi:10.3847/1538-4357/ab042c

Iwasawa, K., Sanders, D. B., Teng, S. H., U, V., Armus, L., Evans, A. S., et al. (2011). C-GOALS: chandra observations of a complete sample of luminous infrared galaxies from the IRAS Revised Bright Galaxy Survey. *A&A* 529, A106. doi:10.1051/0004-6361/201015264

Jaffe, W., Meisenheimer, K., Röttgering, H. J. A., Leinert, C., Richichi, A., Chesneau, O., et al. (2004). The central dusty torus in the active nucleus of NGC 1068. *Nature* 429, 47–49. doi:10.1038/nature02531

Jansen, F., Lumb, D., Altieri, B., Clavel, J., Ehle, M., Erd, C., et al. (2001). XMM-Newton observatory. I. The spacecraft and operations. *A&A* 365, L1–L6. doi:10.1051/0004-6361:20000036

Kaastra, J. S., and Bleeker, J. A. M. (2016). Optimal binning of X-ray spectra and response matrix design. *A&A* 587, A151. doi:10.1051/0004-6361/201527395

Kallová, K., Boorman, P., and Ricci, C. (2023). Investigating model dependencies for obscured Active Galactic Nuclei: a case study of NGC 3982. *In prep*. ApJ.

Kammoun, E., Lohfink, A. M., Masterson, M., Wilkins, D. R., Zhao, X., Baloković, M., et al. (2023). *The High Energy X-ray Probe (HEX-P): probing the physics of the X-ray corona in active galactic nuclei. arXiv e-prints* , arXiv:2311.04679. doi:10.48550/arXiv.2311.04679

Kammoun, E. S., Miller, J. M., Koss, M., Oh, K., Zoghbi, A., Mushotzky, R. F., et al. (2020). A hard look at local, optically selected, obscured seyfert galaxies. *ApJ* 901, 161. doi:10.3847/1538-4357/abb29f

Kammoun, E. S., Miller, J. M., Zoghbi, A., Oh, K., Koss, M., Mushotzky, R. F., et al. (2019). A hard look at NGC 5347: revealing a nearby compton-thick AGN. *ApJ* 877, 102. doi:10.3847/1538-4357/ab1c5f

Kawamuro, T., Ueda, Y., Tazaki, F., Terashima, Y., Mushotzky, R., Mori, M., et al. (2016). Low-luminosity active galactic nuclei as observed with suzaku. *Astrophysical J.* 831, 37. doi:10.3847/0004-637X/831/1/37

Kayal, A., Singh, V., Ricci, C., Mithun, N. P. S., Vadawale, S., Dewangan, G., et al. (2023). Multi-epoch hard X-ray view of compton-thick AGN Circinus galaxy. *MNRAS* 522, 4098–4115. doi:10.1093/mnras/stad1216

Kerzendorf, W. E., Vogl, C., Buchner, J., Contardo, G., Williamson, M., and van der Smagt, P. (2021). Dalek: a deep learning emulator for tardis. *ApJ* 910, L23. doi:10.3847/2041-8213/abeb1b

Kondratko, P. T., Greenhill, L. J., and Moran, J. M. (2008). The parsec-scale accretion disk in NGC 3393. *ApJ* 678, 87–95. doi:10.1086/586879

Körding, E. G., Jester, S., and Fender, R. (2006). Accretion states and radio loudness in active galactic nuclei: analogies with X-ray binaries. *MNRAS* 372, 1366–1378. doi:10.1111/j.1365-2966.2006.10954.x

Koss, M. J., Assef, R., Baloković, M., Stern, D., Gandhi, P., Lamperti, I., et al. (2016). A new population of compton-thick AGNs identified using the spectral curvature above 10 keV. *ApJ* 825, 85. doi:10.3847/0004-637X/825/2/85

Koss, M. J., Romero-Cañizales, C., Baronchelli, L., Teng, S. H., Baloković, M., Puccetti, S., et al. (2015). Broadband observations of the compton-thick nucleus of NGC 3393. *ApJ* 807, 149. doi:10.1088/0004-637X/807/2/149

Kuo, C. Y., Braatz, J. A., Condon, J. J., Impellizzeri, C. M. V., Lo, K. Y., Zaw, I., et al. (2011). The megamaser cosmology project. III. Accurate masses of seven supermassive black holes in active galaxies with circumnuclear megamaser disks. *ApJ* 727, 20. doi:10.1088/0004-637X/727/1/20

La Caria, M. M., Vignali, C., Lanzuisi, G., Gruppioni, C., and Pozzi, F. (2019). Broad-band X-ray analysis of local mid-infrared-selected Compton-thick AGN candidates. *MNRAS* 487, 1662–1674. doi:10.1093/mnras/stz1381

Laha, S., Markowitz, A. G., Krumpe, M., Nikutta, R., Rothschild, R., and Saha, T. (2020). The variable and non-variable X-ray absorbers in compton-thin type II active galactic nuclei. *ApJ* 897, 66. doi:10.3847/1538-4357/ab92ab

LaMassa, S. M., Yaqoob, T., Boorman, P. G., Tzanavaris, P., Levenson, N. A., Gandhi, P., et al. (2019). NuSTAR uncovers an extremely local compton-thick AGN in NGC 4968. *ApJ* 887, 173. doi:10.3847/1538-4357/ab552c

LaMassa, S. M., Yaqoob, T., Levenson, N. A., Boorman, P., Heckman, T. M., Gandhi, P., et al. (2017). Chandra reveals heavy obscuration and circumnuclear star formation in seyfert 2 galaxy NGC 4968. *ApJ* 835, 91. doi:10.3847/1538-4357/835/1/91

LaMassa, S. M., Yaqoob, T., Tzanavaris, P., Gandhi, P., Heckman, T., Lansbury, G., et al. (2023). The complex X-ray obscuration environment in the radio-loud type 2 quasar 3C 223. *ApJ* 944, 152. doi:10.3847/1538-4357/acb3bb

Lansbury, G. B., Gandhi, P., Alexander, D. M., Assef, R. J., Aird, J., Annuar, A., et al. (2015). NuSTAR reveals extreme absorption in z < 0.5 type 2 quasars. *ApJ* 809, 115. doi:10.1088/0004-637X/809/2/115

Lansbury, G. B., Stern, D., Aird, J., Alexander, D. M., Fuentes, C., Harrison, F. A., et al. (2017). The NuSTAR serendipitous survey: the 40-month catalog and the properties of the distant high-energy X-ray source population. *ApJ* 836, 99. doi:10.3847/1538-4357/836/1/99

Laureijs, R., Amiaux, J., Arduini, S., Auguères, J. L., Brinchmann, J., Cole, R., et al. (2011). *Euclid definition study report. arXiv e-prints* , arXiv:1110.3193. doi:10.48550/arXiv.1110.3193

Lefkir, M., Kammoun, E., Barret, D., Boorman, P., Matzeu, G., Miller, J. M., et al. (2023). A hard look at the X-ray spectral variability of NGC 7582. *MNRAS* 522, 1169–1182. doi:10.1093/mnras/stad995

Lehmer, B. D., Garofali, K., Binder, B. A., Fornasini, F., Vulic, N., Zezas, A., et al. (2023). *The high energy X-ray probe: resolved X-ray populations in extragalactic environments. arXiv e-prints* , arXiv:2311.04735. doi:10.48550/arXiv.2311.04735

Levenson, N. A., Krolik, J. H., Życki, P. T., Heckman, T. M., Weaver, K. A., Awaki, H., et al. (2002). Extreme X-ray iron lines in active galactic nuclei. *ApJ* 573, L81–L84. doi:10.1086/342092

Liu, J., Hönig, S. F., Ricci, C., and Paltani, S. (2019). X-ray signatures of the polar dusty gas in AGN. *MNRAS* 490, 4344–4352. doi:10.1093/mnras/stz2908

Liu, Y., and Li, X. (2014). An X-ray spectral model for clumpy tori in active galactic nuclei. *ApJ* 787, 52. doi:10.1088/0004-637X/787/1/52

Maccagni, F. M., Serra, P., Gaspari, M., Kleiner, D., Morokuma-Matsui, K., Oosterloo, T. A., et al. (2021). AGN feeding and feedback in Fornax A. Kinematical analysis of the multi-phase ISM. *A&A* 656, A45. doi:10.1051/0004-6361/202141143

Madsen, K., García, J., Grefenstette, B., Stern, D., and The HEX-P Team (2023). *In prep*. Frontiers in Astronomy and Space Sciences.

Madsen, K. K., Harrison, F. A., Markwardt, C. B., An, H., Grefenstette, B. W., Bachetti, M., et al. (2015). Calibration of the NuSTAR high-energy focusing X-ray telescope. *ApJS* 220, 8. doi:10.1088/0067-0049/220/1/8

Maoz, D., Nagar, N. M., Falcke, H., and Wilson, A. S. (2005). The murmur of the sleeping black hole: detection of nuclear ultraviolet variability in LINER galaxies. *Astrophysical J.* 625, 699–715. doi:10.1086/429795

Marchesi, S., Ajello, M., Marcotulli, L., Comastri, A., Lanzuisi, G., and Vignali, C. (2018). Compton-thick AGNs in the NuSTAR era. *ApJ* 854, 49. doi:10.3847/1538-4357/aaa410

Marchesi, S., Ajello, M., Zhao, X., Comastri, A., La Parola, V., and Segreto, A. (2019a). Compton-thick AGNs in the NuSTAR era. V. Joint NuSTAR and XMM-Newton spectral analysis of three "soft-gamma" candidate CT-AGNs in the swift/BAT 100-month catalog. *ApJ* 882, 162. doi:10.3847/1538-4357/ab340a

Marchesi, S., Ajello, M., Zhao, X., Marcotulli, L., Baloković, M., Brightman, M., et al. (2019b). Compton-thick AGNs in the NuSTAR era. III. A systematic study of the torus covering factor. *ApJ* 872, 8. doi:10.3847/1538-4357/aafbeb

Marchesi, S., Tremblay, L., Ajello, M., Marcotulli, L., Paggi, A., Cusumano, G., et al. (2017). Chandra and NuSTAR follow-up observations of swift-BAT-selected AGNs. *ApJ* 848, 53. doi:10.3847/1538-4357/aa8ee6

Marchesi, S., Zhao, X., Torres-Albà, N., Ajello, M., Gaspari, M., Pizzetti, A., et al. (2022). Compton-thick AGN in the NuSTAR era. VIII. A joint NuSTAR-XMM-Newton monitoring of the changing-look compton-thick AGN NGC 1358. *ApJ* 935, 114. doi:10.3847/1538-4357/ac80be

Marcotulli, L., Ajello, M., Böttcher, M., Coppi, P., Costamante, L., Di Gesu, L., et al. (2023). *The High Energy X-ray Probe (HEX-P): the most powerful jets through the lens of a superb X-ray eye. arXiv e-prints* , arXiv:2311.04801. doi:10.48550/arXiv.2311.04801

Marinucci, A., Bianchi, S., Matt, G., Alexander, D. M., Baloković, M., Bauer, F. E., et al. (2016). NuSTAR catches the unveiling nucleus of NGC 1068. *MNRAS* 456, L94–L98. doi:10.1093/mnrasl/slv178

Markowitz, A. G., Krumpe, M., and Nikutta, R. (2014). First X-ray-based statistical tests for clumpy-torus models: eclipse events from 230 years of monitoring of Seyfert AGN. *MNRAS* 439, 1403–1458. doi:10.1093/mnras/stt2492

Masini, A., Comastri, A., Baloković, M., Zaw, I., Puccetti, S., Ballantyne, D. R., et al. (2016). NuSTAR observations of water megamaser AGN. *A&A* 589, A59. doi:10.1051/0004-6361/201527689

Masini, A., Comastri, A., Hickox, R. C., Koss, M., Civano, F., Brigthman, M., et al. (2019). Measuring the obscuring column of a disk megamaser AGN in a nearby merger. *ApJ* 882, 83. doi:10.3847/1538-4357/ab3214

Masini, A., Comastri, A., Puccetti, S., Baloković, M., Gandhi, P., Guainazzi, M., et al. (2017). The Phoenix galaxy as seen by NuSTAR. *A&A* 597, A100. doi:10.1051/0004-6361/201629444

Matt, G., Fabian, A. C., Guainazzi, M., Iwasawa, K., Bassani, L., and Malaguti, G. (2000). The X-ray spectra of Compton-thick Seyfert 2 galaxies as seen by BeppoSAX. *MNRAS* 318, 173–179. doi:10.1046/j.1365-8711.2000.03721.x

Matzeu, G. A., Braito, V., Reeves, J. N., Severgnini, P., Ballo, L., Caccianiga, A., et al. (2019). Evidence for a clumpy disc-wind in the star-forming Seyfert 2 galaxy MCG-03-58-007. *MNRAS* 483, 2836–2850. doi:10.1093/mnras/sty3327

Matzeu, G. A., Lieu, M., Costa, M. T., Reeves, J. N., Braito, V., Dadina, M., et al. (2022). A new emulated Monte Carlo radiative transfer disc-wind model: X-Ray Accretion Disc-wind Emulator - XRADE. *MNRAS* 515, 6172–6190. doi:10.1093/mnras/stac2155

McConnell, N. J., and Ma, C.-P. (2013). Revisiting the scaling relations of black hole masses and host galaxy properties. *ApJ* 764, 184. doi:10.1088/0004-637X/764/2/184

McKaig, J., Ricci, C., Paltani, S., and Satyapal, S. (2022). X-ray simulations of polar gas in accreting supermassive black holes. *MNRAS* 512, 2961–2971. doi:10.1093/mnras/stab3178

McKinney, W. (2010). "Data structures for statistical computing in Python," in *Proceedings of the 9th Python in science conference*. Editors S. van der Walt, and J. Millman, 56–61. doi:10.25080/Majora-92bf1922-00a

Meidinger, N., Albrecht, S., Beitler, C., Bonholzer, M., Emberger, V., Frank, J., et al. (2020). "Development status of the wide field imager instrument for Athena," in Society of Photo-Optical Instrumentation Engineers (SPIE) Conference Series, 114440T. doi:10.1117/12.2560507

Mohanadas, P., and Annuar, A. (2023). NGC 4117: a new compton-thick AGN revealed by broadband X-ray spectral analysis. *Res. Astronomy Astrophysics* 23, 055002. doi:10.1088/1674-4527/acc151

Moran, E. C., Shahinyan, K., Sugarman, H. R., Vélez, D. O., and Eracleous, M. (2014). Black holes at the centers of nearby dwarf galaxies. *AJ* 148, 136. doi:10.1088/0004-6256/148/6/136

Moravec, E., Svoboda, J., Borkar, A., Boorman, P., Kynoch, D., Panessa, F., et al. (2022). Do radio active galactic nuclei reflect X-ray binary spectral states? *A&A* 662, A28. doi:10.1051/0004-6361/202142870

Murphy, K. D., and Yaqoob, T. (2009). An X-ray spectral model for Compton-thick toroidal reprocessors. *MNRAS* 397, 1549–1562. doi:10.1111/j.1365-2966.2009.15025.x

Nagar, N. M., Falcke, H., Wilson, A. S., and Ho, L. C. (2005). Accretion disk model for low-luminosity active galactic nuclei. *Astrophysical J.* 620, 83–89. doi:10.1086/427175

Nandra, K., Barret, D., Barcons, X., Fabian, A., den Herder, J.-W., Piro, L., et al. (2013). *The hot and energetic Universe: a white paper presenting the science theme motivating the Athena+ mission. arXiv e-prints* , arXiv:1306.2307. doi:10.48550/arXiv.1306.2307

Nardini, E. (2017). Nuclear absorption and emission in the AGN merger NGC 6240: the hard X-ray view. *MNRAS* 471, 3483–3493. doi:10.1093/mnras/stx1878

Nemmen, R. S., Storchi-Bergmann, T., and Eracleous, M. (2014). Spectral models for low-luminosity active galactic nuclei in LINERs: the role of advection-dominated accretion and jets. *MNRAS* 438, 2804–2827. doi:10.1093/mnras/stt2388

Nemmen, R. S., Storchi-Bergmann, T., Yuan, F., Eracleous, M., Terashima, Y., and Wilson, A. S. (2006). Radiatively inefficient accretion flow in the nucleus of NGC 1097. *Astrophysical J.* 643, 652–659. doi:10.1086/500571

Nenkova, M., Sirocky, M. M., Ivezić, Ž., and Elitzur, M. (2008). AGN dusty tori. I. Handling of clumpy media. *ApJ* 685, 147–159. doi:10.1086/590482

Netzer, H. (2015). Revisiting the unified model of active galactic nuclei. *ARA&A* 53, 365–408. doi:10.1146/annurev-astro-082214-122302

Odaka, H., Aharonian, F., Watanabe, S., Tanaka, Y., Khangulyan, D., and Takahashi, T. (2011). X-ray diagnostics of giant molecular clouds in the galactic center region and past activity of sgr A. *ApJ* 740, 103. doi:10.1088/0004-637X/740/2/103

Odaka, H., Yoneda, H., Takahashi, T., and Fabian, A. (2016). Sensitivity of the Fe Kα Compton shoulder to the geometry and variability of the X-ray illumination of cosmic objects. *MNRAS* 462, 2366–2381. doi:10.1093/mnras/stw1764

Osorio-Clavijo, N., González-Martín, O., Sánchez, S. F., Esparza-Arredondo, D., Masegosa, J., Victoria-Ceballos, C., et al. (2022). Observational hints on the torus obscuring gas behaviour through X-rays with NuSTAR data. *MNRAS* 510, 5102–5118. doi:10.1093/mnras/stab3752

Paltani, S., and Ricci, C. (2017). RefleX: X-ray absorption and reflection in active galactic nuclei for arbitrary geometries. *A&A* 607, A31. doi:10.1051/0004-6361/201629623

Panessa, F., Castangia, P., Malizia, A., Bassani, L., Tarchi, A., Bazzano, A., et al. (2020). Water megamaser emission in hard X-ray selected AGN. *A&A* 641, A162. doi:10.1051/0004-6361/201937407

Pfeifle, R. W., Boorman, P. G., Weaver, K. A., Buchner, J., Civano, F., Madsen, K., et al. (2023). *The high energy X-ray probe (HEX-P): the future of hard X-ray dual AGN science. arXiv e-prints* , arXiv:2311.05154. doi:10.48550/arXiv.2311.05154

Piotrowska, J. M., García, J. A., Walton, D. J., Beckmann, R. S., Stern, D., Ballantyne, D. R., et al. (2023). *The high energy X-ray probe (HEX-P): constraining supermassive black hole growth with population spin measurements. arXiv e-prints* , arXiv:2311.04752. doi:10.48550/arXiv.2311.04752

Pizzetti, A., Torres-Albà, N., Marchesi, S., Ajello, M., Silver, R., and Zhao, X. (2022). A multiepoch X-ray study of the nearby seyfert 2 galaxy NGC 7479: linking column density variability to the torus geometry. *ApJ* 936, 149. doi:10.3847/1538-4357/ac86c6

Ptak, A., Hornschemeier, A., Zezas, A., Lehmer, B., Yukita, M., Wik, D., et al. (2015). A focused, hard X-ray look at arp 299 with NuSTAR. *ApJ* 800, 104. doi:10.1088/0004-637X/800/2/104

Puccetti, S., Comastri, A., Bauer, F. E., Brandt, W. N., Fiore, F., Harrison, F. A., et al. (2016). Hard X-ray emission of the luminous infrared galaxy NGC 6240 as observed by NuSTAR. *A&A* 585, A157. doi:10.1051/0004-6361/201527189

Puccetti, S., Comastri, A., Fiore, F., Arévalo, P., Risaliti, G., Bauer, F. E., et al. (2014). The variable hard X-ray emission of NGC 4945 as observed by NuSTAR. *ApJ* 793, 26. doi:10.1088/0004-637X/793/1/26

Racca, G. D., Laureijs, R., Stagnaro, L., Salvignol, J.-C., Lorenzo Alvarez, J., Saavedra Criado, G., et al. (2016). "The Euclid mission design," in *Space telescopes and instrumentation 2016: optical, infrared, and millimeter wave*. Editors H. A. MacEwen, G. G. Fazio, M. Lystrup, N. Batalha, N. Siegler, and E. C. Tong, 99040O. doi:10.1117/12.2230762

Ramos Almeida, C., and Ricci, C. (2017). Nuclear obscuration in active galactic nuclei. *Nat. Astron.* 1, 679–689. doi:10.1038/s41550-017-0232-z

Reines, A. E. (2022). Hunting for massive black holes in dwarf galaxies. *Nat. Astron.* 6, 26–34. doi:10.1038/s41550-021-01556-0

Reines, A. E., Greene, J. E., and Geha, M. (2013). Dwarf galaxies with optical signatures of active massive black holes. *ApJ* 775, 116. doi:10.1088/0004-637X/775/2/116

Reynolds, C. S., Lohfink, A. M., Ogle, P. M., Harrison, F. A., Madsen, K. K., Fabian, A. C., et al. (2015). NuSTAR observations of the powerful radio galaxy Cygnus A. *ApJ* 808, 154. doi:10.1088/0004-637X/808/2/154

Ricci, C., Ananna, T. T., Temple, M. J., Urry, C. M., Koss, M. J., Trakhtenbrot, B., et al. (2022). BASS XXXVII: the role of radiative feedback in the growth and obscuration properties of nearby supermassive black holes. *ApJ* 938, 67. doi:10.3847/1538-4357/ac8e67

Ricci, C., Bauer, F. E., Arevalo, P., Boggs, S., Brandt, W. N., Christensen, F. E., et al. (2016). IC 751: a new changing look AGN discovered by NuSTAR. *ApJ* 820, 5. doi:10.3847/0004-637X/820/1/5

Ricci, C., Bauer, F. E., Treister, E., Schawinski, K., Privon, G. C., Blecha, L., et al. (2017). Growing supermassive black holes in the late stages of galaxy mergers are heavily obscured. *MNRAS* 468, stx173–1299. doi:10.1093/mnras/stx173

Ricci, C., and Paltani, S. (2023). Ray-tracing simulations and spectral models of X-ray radiation in dusty media. *ApJ* 945, 55. doi:10.3847/1538-4357/acb5a6

Ricci, C., Privon, G. C., Pfeifle, R. W., Armus, L., Iwasawa, K., Torres-Albà, N., et al. (2021). A hard X-ray view of luminous and ultra-luminous infrared galaxies in GOALS - I. AGN obscuration along the merger sequence. *MNRAS* 506, 5935–5950. doi:10.1093/mnras/stab2052

Ricci, C., and Trakhtenbrot, B. (2022). *Changing-look active galactic nuclei. arXiv e-prints* , arXiv:2211.05132. doi:10.48550/arXiv.2211.05132

Ricci, C., Trakhtenbrot, B., Koss, M. J., Ueda, Y., Del Vecchio, I., Treister, E., et al. (2017c). BAT AGN spectroscopic survey. V. X-ray properties of the swift/BAT 70-month AGN catalog. *ApJS* 233, 17. doi:10.3847/1538-4365/aa96ad

Ricci, C., Trakhtenbrot, B., Koss, M. J., Ueda, Y., Schawinski, K., Oh, K., et al. (2017d). The close environments of accreting massive black holes are shaped by radiative feedback. *Nature* 549, 488–491. doi:10.1038/nature23906

Ricci, C., Ueda, Y., Koss, M. J., Trakhtenbrot, B., Bauer, F. E., and Gandhi, P. (2015). Compton-thick accretion in the local universe. *ApJ* 815, L13. doi:10.1088/2041-8205/815/1/L13

Rieke, G. H., Wright, G. S., Böker, T., Bouwman, J., Colina, L., Glasse, A., et al. (2015). The mid-infrared instrument for the James Webb space telescope, I: introduction. *PASP* 127, 584–594. doi:10.1086/682252

Rino-Silvestre, J., González-Gaitán, S., Stalevski, M., Smole, M., Guilherme-Garcia, P., Carvalho, J. P., et al. (2022). *EmulART: emulating Radiative Transfer – a pilot study on autoencoder based dimensionality reduction for radiative transfer models. arXiv e-prints*, arXiv:2210.15400. doi:10.48550/arXiv.2210.15400

Risaliti, G., Elvis, M., Fabbiano, G., Baldi, A., and Zezas, A. (2005). Rapid compton-thick/compton-thin transitions in the seyfert 2 galaxy NGC 1365. *ApJ* 623, L93–L96. doi:10.1086/430252

Risaliti, G., Elvis, M., Fabbiano, G., Baldi, A., Zezas, A., and Salvati, M. (2007). Occultation measurement of the size of the X-ray-emitting region in the active galactic nucleus of NGC 1365. *ApJ* 659, L111–L114. doi:10.1086/517884

Risaliti, G., Elvis, M., and Nicastro, F. (2002). Ubiquitous variability of X-ray-absorbing column densities in seyfert 2 galaxies. *ApJ* 571, 234–246. doi:10.1086/324146

Risaliti, G., Maiolino, R., and Salvati, M. (1999). The distribution of absorbing column densities among seyfert 2 galaxies. *ApJ* 522, 157–164. doi:10.1086/307623

Risaliti, G., Salvati, M., Elvis, M., Fabbiano, G., Baldi, A., Bianchi, S., et al. (2009). The XMM-Newton long look of NGC 1365: uncovering of the obscured X-ray source. *MNRAS* 393, L1–L5. doi:10.1111/j.1745-3933.2008.00580.x

Rivers, E., Baloković, M., Arévalo, P., Bauer, F. E., Boggs, S. E., Brandt, W. N., et al. (2015). The NuSTAR view of reflection and absorption in NGC 7582. *ApJ* 815, 55. doi:10.1088/0004-637X/815/1/55

Rose, T., Edge, A. C., Combes, F., Gaspari, M., Hamer, S., Nesvadba, N., et al. (2019). Constraining cold accretion on to supermassive black holes: molecular gas in the cores of eight brightest cluster galaxies revealed by joint CO and CN absorption. *MNRAS* 489, 349–365. doi:10.1093/mnras/stz2138

Saade, M. L., Brightman, M., Stern, D., Malkan, M. A., and García, J. A. (2022). NuSTAR observations of AGNs with low observed X-ray to [O III] luminosity ratios: heavily obscured AGNs or turned-off AGNs? *ApJ* 936, 162. doi:10.3847/1538-4357/ac88cf

Saha, T., Markowitz, A. G., and Buchner, J. (2022). Inferring the morphology of AGN torus using X-ray spectra: a reliability study. *MNRAS* 509, 5485–5510. doi:10.1093/mnras/stab3250

Sartori, L. F., Schawinski, K., Koss, M. J., Ricci, C., Treister, E., Stern, D., et al. (2018). Joint NuSTAR and Chandra analysis of the obscured quasar in IC 2497 - hanny's Voorwerp system. *MNRAS* 474, 2444–2451. doi:10.1093/mnras/stx2952

Semena, A. N., Sazonov, S. Y., and Krivonos, R. A. (2019). Spectral properties of heavily obscured seyfert galaxies from the INTEGRAL all-sky survey. *Astron. Lett.* 45, 490–520. doi:10.1134/S1063773719080085

Sengupta, D., Marchesi, S., Vignali, C., Torres-Albà, N., Bertola, E., Pizzetti, A., et al. (2023). Compton-thick AGN in the NuSTAR era X: analysing seven local CT-AGN candidates. *A&A* 676, A103. doi:10.1051/0004-6361/202245646

Shakura, N. I., and Sunyaev, R. A. (1973). Black holes in binary systems. Observational appearance. *A&A* 24, 337–355.

Silver, R., Torres-Albà, N., Zhao, X., Marchesi, S., Pizzetti, A., Cox, I., et al. (2022). Compton-thick AGN in the NuSTAR era. IX. A joint NuSTAR and xmm-Newton analysis of four local AGN. *ApJ* 940, 148. doi:10.3847/1538-4357/ac9bf8

Spergel, D., Gehrels, N., Baltay, C., Bennett, D., Breckinridge, J., Donahue, M., et al. (2015). *Wide-field InfrarRed survey telescope-astrophysics focused telescope assets WFIRST-AFTA 2015 report. arXiv e-prints* , arXiv:1503.03757. doi:10.48550/arXiv.1503.03757

Springel, V., Di Matteo, T., and Hernquist, L. (2005). Modelling feedback from stars and black holes in galaxy mergers. *MNRAS* 361, 776–794. doi:10.1111/j.1365-2966.2005.09238.x

Storchi-Bergmann, T., and Schnorr-Müller, A. (2019). Observational constraints on the feeding of supermassive black holes. *Nat. Astron.* 3, 48–61. doi:10.1038/s41550-018-0611-0

Svoboda, J., Guainazzi, M., and Merloni, A. (2017). AGN spectral states from simultaneous UV and X-ray observations by XMM-Newton. *A&A* 603, A127. doi:10.1051/0004-6361/201630181

Tanimoto, A., Ueda, Y., Odaka, H., Kawaguchi, T., Fukazawa, Y., and Kawamuro, T. (2019). XCLUMPY: X-ray spectral model from clumpy torus and its application to the Circinus galaxy. *ApJ* 877, 95. doi:10.3847/1538-4357/ab1b20

Tanimoto, A., Ueda, Y., Odaka, H., Ogawa, S., Yamada, S., Kawaguchi, T., et al. (2020). Application of an X-ray clumpy torus model (XCLUMPY) to 10 obscured active galactic nuclei observed with suzaku and NuSTAR. *ApJ* 897, 2. doi:10.3847/1538-4357/ab96bc

Tanimoto, A., Ueda, Y., Odaka, H., Yamada, S., and Ricci, C. (2022). NuSTAR observations of 52 compton-thick active galactic nuclei selected by the swift/burst Alert telescope all-sky hard X-ray survey. *ApJS* 260, 30. doi:10.3847/1538-4365/ac5f59

Temi, P., Gaspari, M., Brighenti, F., Werner, N., Grossova, R., Gitti, M., et al. (2022). Probing multiphase gas in local massive elliptical galaxies via multiwavelength observations. *ApJ* 928, 150. doi:10.3847/1538-4357/ac5036

Teng, S. H., Rigby, J. R., Stern, D., Ptak, A., Alexander, D. M., Bauer, F. E., et al. (2015). A NuSTAR survey of nearby ultraluminous infrared galaxies. *ApJ* 814, 56. doi:10.1088/0004-637X/814/1/56

Terashima, Y. (2002). Asca observations of "type 2" liners: evidence for a stellar source of ionization. *Astrophysical J.* 576, 653–666. doi:10.1086/341772

Torres-Albà, N., Iwasawa, K., Díaz-Santos, T., Charmandaris, V., Ricci, C., Chu, J. K., et al. (2018). C-GOALS. II. Chandra observations of the lower luminosity sample of nearby luminous infrared galaxies in GOALS. *A&A* 620, A140. doi:10.1051/0004-6361/201834105

Torres-Albà, N., Marchesi, S., Zhao, X., Ajello, M., Silver, R., Ananna, T. T., et al. (2021). Compton-thick AGN in the NuSTAR era VI: the observed compton-thick fraction in the local universe. *ApJ* 922, 252. doi:10.3847/1538-4357/ac1c73

Torres-Albà, N., Marchesi, S., Zhao, X., Cox, I., Pizzetti, A., Ajello, M., et al. (2023). *Hydrogen column density variability in a sample of local compton-thin AGN*. *arXiv e-prints* , arXiv:2301.07138. doi:10.48550/arXiv.2301.07138

Traina, A., Marchesi, S., Vignali, C., Torres-Albà, N., Ajello, M., Pizzetti, A., et al. (2021). Compton-thick AGN in the NuSTAR era VII. A joint NuSTAR, chandra, and xmm-Newton analysis of two nearby, heavily obscured sources. *ApJ* 922, 159. doi:10.3847/1538-4357/ac1fee

Treister, E., Urry, C. M., and Virani, S. (2009). The space density of compton-thick active galactic nucleus and the X-ray background. *ApJ* 696, 110–120. doi:10.1088/0004-637X/696/1/110

Trump, J. R., Impey, C. D., Kelly, B. C., Civano, F., Gabor, J. M., Diamond-Stanic, A. M., et al. (2011). Mid-infrared selection of active galactic nuclei with the wide-field infrared survey explorer. i. characterizing wise-selected agns in cosmos. *Astrophysical J.* 733, 60. doi:10.1088/0004-637X/733/1/60

Trump, J. R., Sun, M., Zeimann, G. R., Luck, C., Bridge, J. S., Grier, C. J., et al. (2015). The biases of optical line-ratio selection for active galactic nuclei and the intrinsic relationship between black hole accretion and galaxy star formation. *ApJ* 811, 26. doi:10.1088/0004-637X/811/1/26

Turner, T. J., Reeves, J. N., Braito, V., Yaqoob, T., Kraemer, S. B., and Severgnini, P. (2020). Elucidating the global distribution of reprocessing gas in NGC 1194. *MNRAS* 498, 1983–1991. doi:10.1093/mnras/staa2401

Ueda, Y., Akiyama, M., Hasinger, G., Miyaji, T., and Watson, M. G. (2014). Toward the standard population synthesis model of the X-ray background: evolution of X-ray luminosity and absorption functions of active galactic nuclei including compton-thick populations. *ApJ* 786, 104. doi:10.1088/0004-637X/786/2/104

Uematsu, R., Ueda, Y., Tanimoto, A., Kawamuro, T., Setoguchi, K., Ogawa, S., et al. (2021). X-ray constraint on the location of the AGN torus in the Circinus galaxy. *ApJ* 913, 17. doi:10.3847/1538-4357/abf0a2

Urry, C. M., and Padovani, P. (1995). Unified schemes for radio-loud active galactic nuclei. *PASP* 107, 803. doi:10.1086/133630

Ursini, F., Boissay-Malaquin, R., Marinucci, A., Matt, G., Bianchi, S., Capalbi, M., et al. (2015). Simultaneous x-ray/optical/uv snapshots of active galactic nuclei from xmm-Newton: spectral energy distributions for the reverberation mapped sample. *Mon. Notices R. Astronomical Soc.* 452, 3266–3272. doi:10.1093/mnras/stv1527

Vander Meulen, B., Camps, P., Stalevski, M., and Baes, M. (2023). *X-ray radiative transfer in full 3D with SKIRT*. *arXiv e-prints* , arXiv:2304.10563. doi:10.48550/arXiv.2304.10563

van Dyk, D. A., Connors, A., Kashyap, V. L., and Siemiginowska, A. (2001). Analysis of energy spectra with low photon counts via bayesian posterior simulation. *ApJ* 548, 224–243. doi:10.1086/318656

Vasudevan, R. V., Brandt, W. N., Mushotzky, R. F., Winter, L. M., Baumgartner, W. H., Shimizu, T. T., et al. (2013). X-ray properties of the northern galactic cap sources in the 58 Month swift/BAT catalog. *ApJ* 763, 111. doi:10.1088/0004-637X/763/2/111

Vasudevan, R. V., Fabian, A. C., Reynolds, C. S., Aird, J., Dauser, T., and Gallo, L. C. (2016). A selection effect boosting the contribution from rapidly spinning black holes to the cosmic X-ray background. *MNRAS* 458, 2012–2023. doi:10.1093/mnras/stw363

Vasylenko, A. A., Fedorova, E., and Zhdanov, V. I. (2013). Observations of Sy2 galaxy NGC 3281 by XMM-Newton and INTEGRAL satellites. *Adv. Astronomy Space Phys.* 3, 120–125. doi:10.48550/arXiv.1311.1691

Vignali, C., Severgnini, P., Piconcelli, E., Lanzuisi, G., Gilli, R., Mignoli, M., et al. (2018). NuSTAR reveals that the heavily obscured nucleus of NGC 2785 was the contaminant of IRAS 09104+4109 in the BeppoSAX/PDS hard X-rays. *A&A* 619, A16. doi:10.1051/0004-6361/201833805

Virtanen, P., Gommers, R., Oliphant, T. E., Haberland, M., Reddy, T., Cournapeau, D., et al. (2020). SciPy 1.0: fundamental algorithms for scientific computing in Python. *Nat. Methods* 17, 261–272. doi:10.1038/s41592-019-0686-2

Vollmer, B., and Duschl, W. J. (2002). The dynamics of the circumnuclear disk and its environment in the galactic centre. *A&A* 388, 128–148. doi:10.1051/0004-6361:20020422

Volonteri, M. (2010). Formation of supermassive black holes. *A&A Rev.* 18, 279–315. doi:10.1007/s00159-010-0029-x

Volonteri, M., Lodato, G., and Natarajan, P. (2008). The evolution of massive black hole seeds. *MNRAS* 383, 1079–1088. doi:10.1111/j.1365-2966.2007.12589.x

Wada, K. (2012). Radiation-driven fountain and origin of torus around active galactic nuclei. *ApJ* 758, 66. doi:10.1088/0004-637X/758/1/66

Walton, D. J., Risaliti, G., Harrison, F. A., Fabian, A. C., Miller, J. M., Arevalo, P., et al. (2014). NuSTAR and XMM-Newton observations of NGC 1365: extreme absorption variability and a constant inner accretion disk. *ApJ* 788, 76. doi:10.1088/0004-637X/788/1/76

Williams, D. R. A., Pahari, M., Baldi, R. D., McHardy, I. M., Mathur, S., Beswick, R. J., et al. (2022). LeMMINGs - IV. The X-ray properties of a statistically complete sample of the nuclei in active and inactive galaxies from the Palomar sample. *MNRAS* 510, 4909–4928. doi:10.1093/mnras/stab3310

Yamada, S., Ueda, Y., Tanimoto, A., Imanishi, M., Toba, Y., Ricci, C., et al. (2021). Comprehensive broadband X-ray and multiwavelength study of active galactic nuclei in 57 local luminous and ultraluminous infrared galaxies observed with NuSTAR and/or swift/BAT. *ApJS* 257, 61. doi:10.3847/1538-4365/ac17f5

Yamada, S., Ueda, Y., Tanimoto, A., Oda, S., Imanishi, M., Toba, Y., et al. (2020). Nature of compton-thick active galactic nuclei in "nonmerging" luminous infrared galaxies UGC 2608 and NGC 5135 revealed with broadband X-ray spectroscopy. *ApJ* 897, 107. doi:10.3847/1538-4357/ab94b1

Yamauchi, A., Nakai, N., Ishihara, Y., Diamond, P., and Sato, N. (2012). Water-vapor maser disk at the nucleus of the seyfert 2 galaxy IC 2560 and its distance. *PASJ* 64, 103. doi:10.1093/pasj/64.5.103

Yaqoob, T. (2012). The nature of the Compton-thick X-ray reprocessor in NGC 4945. *MNRAS* 423, 3360–3396. doi:10.1111/j.1365-2966.2012.21129.x

Younes, G., Porquet, D., Sabra, B., Reeves, J. N., and Grosso, N. (2011). Discovery of relativistic fe kα emission in the seyfert 1.9 galaxy mcg-05-23-16. *Astronomy Astrophysics* 530, A149. doi:10.1051/0004-6361/201116806

Younes, G., Porquet, D., Sabra, B., Reeves, J. N., and Grosso, N. (2019). A systematic study of the properties of relativistic fe kα lines in agn. *Astronomy Astrophysics* 628, A56. doi:10.1051/0004-6361/201834282

Young, A. J., McHardy, I. M., Emmanoulopoulos, D., and Nandra, K. (2018). Nustar and xmm-Newton observations of the hard state in the seyfert 1.5 galaxy mcg–5-23-16. *Astrophysical J.* 853, 56. doi:10.3847/1538-4357/aaa5aa

Zaino, A., Bianchi, S., Marinucci, A., Matt, G., Bauer, F. E., Brandt, W. N., et al. (2020). Probing the circumnuclear absorbing medium of the buried AGN in NGC 1068 through NuSTAR observations. *MNRAS* 492, 3872–3884. doi:10.1093/mnras/staa107

Zaw, I., Rosenthal, M. J., Katkov, I. Y., Gelfand, J. D., Chen, Y.-P., Greenhill, L. J., et al. (2020). An accreting, anomalously low-mass black hole at the center of low-mass galaxy IC 750. *ApJ* 897, 111. doi:10.3847/1538-4357/ab9944

Zhao, X., Marchesi, S., and Ajello, M. (2019a). Compton-thick AGN in the NuSTAR era. IV. A deep NuSTAR and xmm-Newton view of the candidate compton-thick AGN in eso 116-g018. *ApJ* 871, 182. doi:10.3847/1538-4357/aaf80b

Zhao, X., Marchesi, S., Ajello, M., Baloković, M., and Fischer, T. (2020). A broadband X-ray study of a sample of AGNs with [O III] measured inclinations. *ApJ* 894, 71. doi:10.3847/1538-4357/ab879d

Zhao, X., Marchesi, S., Ajello, M., Cole, D., Hu, Z., Silver, R., et al. (2021). The properties of the AGN torus as revealed from a set of unbiased NuSTAR observations. *A&A* 650, A57. doi:10.1051/0004-6361/202140297

Zhao, X., Marchesi, S., Ajello, M., Marcotulli, L., Cusumano, G., La Parola, V., et al. (2019b). Compton-thick AGNs in the NuSTAR era. II. A deep NuSTAR and xmm-Newton view of the candidate compton-thick AGN in NGC 1358. *ApJ* 870, 60. doi:10.3847/1538-4357/aaf1a0

ZuHone, J. A., Vikhlinin, A., Tremblay, G. R., Randall, S. W., Andrade-Santos, F., and Bourdin, H. (2023). *SOXS: simulated observations of X-ray sources*. Astrophysics Source Code Library. record ascl:2301.024.